

Decomposition of unsteady sheet/cloud cavitation dynamics in fluid-structure interaction via POD and DMD methods

Yunqing Liu, Qin Wu*, Biao Huang*, Hanzhe Zhang, Wendong Liang, Guoyu Wang

School of Mechanical Engineering, Beijing Institute of Technology, Beijing, China



ARTICLE INFO

Article history:

Received 5 June 2020

Revised 27 March 2021

Accepted 13 May 2021

Available online 6 June 2021

Keywords:

Unsteady sheet/cloud cavitation

Cavitation dynamics

Fluid-structure interaction

POD

DMD

ABSTRACT

The objective of this paper is to study sheet/cloud cavitation dynamics in fluid-structure interaction by experimental and numerical methods. The high-speed camera is applied to observe the cavitating flow structures and the Laser Doppler Vibrometer is used to characterize the vibration. A hydrodynamic load cell is applied to measure the lift and drag static force. The results present different cavitating patterns of the flexible hydrofoil and the vibration amplitude is enhanced when the cloud cavitation occurs. The hybrid coupled fluid structure algorithm is adopted to simulate the cloud cavity shedding downstream due to the re-entrant jet from the cavity closure to the hydrofoil's leading edge. The vibration analysis shows that the frequency spectrum of the flexible hydrofoil is much more complicated than the rigid one, the main cavitating flow-induced vibration frequency of the flexible hydrofoil is due to the cavity shedding, others are corresponding to vortex shedding frequency and natural frequency in water. The Proper Orthogonal Decomposition (POD) and Dynamic Mode Decomposition (DMD) methods are used to investigate the dominant coherent structures of the cavitating flow. With the POD method, it reveals that large-scale cloud cavities occupy a large amount of energy in the flow field. The DMD method accurately extracts the dominant frequency and modal characteristic, with the first mode corresponding to the mean flow field, the second mode being cavity shedding and the third and fourth mode being vortex shedding.

© 2021 Elsevier Ltd. All rights reserved.

1. Introduction

Cavitation generally occurs when the local pressure drops below the saturated vapor pressure with the gas filled or gas and vapor filled cavities formed (Wang et al., 2017; Batchelor, 1967). Some problems such as vibration, noise, erosion, even structural failure is unavoidable with the occurrence of cavitation, so it has become a great issue for many applications, such as hydraulic machinery, marine engineering and naval industry (Peters et al., 2018; Arndt, 1981; Yang et al., 2019). With using lightweight structures in these fields, the elastic deformation of structure cannot be ignored, so the cavitation-structure interaction has become more complex.

Much work has been conducted to study the cavitating flow over rigid hydrofoils. Recent works have studied the unsteady cavitation structures of hydrofoils via experimental (Wu et al., 2018b; Peng et al., 2016; Harwood et al., 2019) and numerical studies (Wang et al., 2018a, 2018b; Wu et al., 2016; Saito et al., 2007; Sun et al., 2019). Wang et al. (2001) experimentally investigated different cavitation regimes around hydrofoils with visualization

and measurement. They showed a distinctly quasi-periodic pattern that in cloud cavitation. To further investigate the cloud cavitation, Kubota et al. (1992) employed experimental and numerical methods to study the cloud cavitation around a hydrofoil. They pointed out that the cloud cavities shed from the trailing edge of the cavities along with large-scale vortices. Huang et al. (2019) reviewed the cavitating flow structures and flow mechanisms. They discussed the evolution of sheet/cloud cavity, along with cavitating vortex street's forming. Leroux et al. (2005) found that re-entrant jet was mainly responsible for the cavity break off. Ji et al. (2013) simulated cloud cavitation around a twisted hydrofoil. The results showed that the cavitation-vortex interaction is the principal mechanism for the evolution of horse-shoe vortexes. The re-entrant jet mechanism is one of the most important factors of the cloud cavitation shedding. Che et al. (2019) experimentally investigated the dynamic behaviors of re-entrant jet in the partial cavity and transitional cavity oscillation. The results showed that in the partial cavity oscillation, the sheet cavitation grew with good spanwise uniformity, but in the transitional cavity oscillation, the cavity grew with a concave line. Pelz et al. (2017) investigated the transition from sheet to cloud cavitation analytically, and a physical model was introduced. They presented the evidence of nucleation and bubble collapse for the growth of the sheet cavity and under-

* Corresponding authors.

E-mail addresses: wuqin919@bit.edu.cn (Q. Wu), huangbiao@bit.edu.cn (B. Huang).

lined the role of wall friction for the evolution of the re-entrant jet. Smith et al. (2020a) studied the influence of fluid-structure interaction on cloud cavitation about a stiff hydrofoil in experimental, numerical and SPOD methods. They found the FSI was only reflected in lock-in phenomena and a strong correction between the tip deformations and spanwise cavity oscillations. So, they claimed that the influence of FSI on the cavitation behavior with the stainless model is almost inconsequential.

In addition to the cavitating flow around rigid hydrofoils, numerous researchers have investigated the effects of cavitation on the flexible hydrofoils. Ducoin and Young (2013) numerically investigated the viscous effects, like transition and stall, on the hydroelastic stability of hydrofoils. They found that viscous effects tend to delay or suppress divergence because the effective angle of attack decreased due to the center of pressure moved toward the midchord at large-scale separating flow. Lelong et al. (2018) conducted an experimental procedure to analyze the cavitating flow around a lightweight hydrofoil with fluid-structure interaction considered. They found that with the development of cavitation, the cavity shedding frequency and the bending mode frequency controlled the structure response. Ducoin et al. (2012a) experimentally investigated the boundary-layer transition induced vibrations on a flexible hydrofoil, the results showed that foil vibrations characteristics in terms of frequency and amplitude depend on the vortex shedding frequency. They (Ducoin et al., 2012b) further found that cavitation induced a large increase of the vibration level due to hydrodynamic load unsteadiness and change of modal response for specific frequencies. Not only the effects of cavitation on the foil, but also the influence of foil on cavitation has been investigated. Chae et al. (2016) presented numerical studies of flow-induce vibration of flexible hydrofoils. The foil vibrations are found to be dominated by the natural frequencies in absence of large-scale vortex shedding due to flow separation. Wu et al. (2018a) compared the cavitation patterns and cavitating flow-induced vibration of steel and flexible hydrofoils. They stated that cavities around the flexible hydrofoil appeared to be fragmentized due to its vibration and the main vibration frequency was dominated by the cavity shedding frequency. Young (2018) conducted experimental and numerical work to study the load-depend bend-twist coupling effects on the hydroelastic response of composite hydrofoils. They pointed at material bend-twist coupling that led to nose-up twist accelerated stall and static divergence. While the opposite is true for material bend-twist coupling led to nose-down twist. Smith et al. (2018) compared the rigid and compliant hydrofoil experimentally to explain many observed phenomena and the extensive research into fluid-structure interaction. They found that the compliance damped the higher frequency force fluctuations while showed strong correction between normal force and tip deflection. Subsequently, Smith et al. (2020b) further analyze the high-speed photography and force measurements on stiff and flexible hydrofoils, they found that the flexibility led to high frequency attenuation of the forces, frequency modulation, accelerated cavitation regime transition as well as multiple lock-in modes.

It's well known that the cavitating flows are quasi periodic instead of real periodic, one cycle is insufficient to describe the hydrodynamic characteristics of the hydrofoil in the computational domain. To extract the dominant coherent features and statistical data of the cavitation flow, POD and DMD have been proposed and applied in a wide of applications, such as orifice plate jet (Alenius, 2014), open cavity flow (Vinha et al., 2016), wave packet (Pan et al., 2015). The POD method is to acquire the most energetic modes of the flow field and use them to reconstruct the flow field. Miyanawala and Jaiman (2019) utilized POD method to analyze the wake flow of a square cylinder under different flow conditions. They utilized POD mode to capture the organized motions of wake flow, the vortex street, the shear layer and the near-wake bubble.

Wang et al. (2018) used POD method to study the ventilated cavitating flow around a bluff body, with focus on the vortex shedding behavior in the wake. The results showed that the first and second mode frequencies, associated with the vortex shedding frequency reduced as the gas entrainment coefficient Q_v increase, the energy of large-scale structures decreased with the increase of Q_v in terms of spatial scales. POD method is effective to determine the most energetic flow structures, however, for the complex cavitating flow, the evolution of cavitation structures is characterized by the obvious dominant frequency, which also includes the low-energy features but with a great influence on the dynamic characteristics of the flow. Dynamic Mode Decomposition method is proposed to present the contribution of the flow structure with different frequencies to the flow field by extracting the dominant frequency of the system. Liu et al. (2019) employed DMD method to analyze the cavitating flow coherent structures around a hydrofoil, they found that the cavitating flow remained stable at the long side due to the dynamic mode mainly occurred on the short side. They also accurately extracted the frequency characteristics in DMD methods. Prothin et al. (2016) used POD and DMD methods to analyze the hydrodynamic instability of sheet cavities around a hydrofoil. They showed that the 3D effects were caused by the re-entrant jet instability or propagating shock wave mechanism at the beginning of the cloud cavitation shedding process. Liang et al. (2020) employed the POD and DMD method to investigate the liquid nitrogen cavitating flows with emphasis on the vortex structures. They compared the thermal modes with the isothermal modes, the results showed the significant difference between the two typical cavitation modes is the positions.

Although the phenomenon and mechanism of cavitation have been investigated, a concise review of previous works shows that the explanation of complex cavitation-induced vibration frequency needs to be further investigated. In addition, the effect of the flexibility on the cavitation regime transition, the forces, deformation, and vibration has not been well explained yet. For this reason, the paper presents the experimental and numerical study of the cloud cavitating flow structures and cavitation-induced vibration on a NACA66 hydrofoil. By comparing the rigid and flexible hydrofoil, the effect of the flexibility on the fluid-structure interaction has been further investigated. Then POD and DMD methods are employed to investigate the association among the unsteady cloud cavity shedding, vortex shedding and corresponding vibrations.

2. Experimental setup

Measurements are conducted in the cavitation tunnel in Beijing Institute of Technology (Wu et al., 2017), as shown in Fig. 1. It is mainly composed of the inlet pipe, the constricted section, the test section, the diffusion section and the return pipe, with the test section 0.7 m long, 0.07 m wide and 0.19 m high, as shown in Fig. 2. The adjustable flow parameters are the upstream pressure (with range of 0–0.095 MPa and control accuracy of 5.3%) and the flow velocity (with range of 0–20 m/s and control accuracy of 0.5%). In addition, the water in the underground reservoir should be fully settled before the experiment to ensure the basic stability of the gas content and cavitation nucleus distribution in the water. A high-speed camera with a sampling frequency of 2500 fps is exploited to observe the cavitation structures. Two dedicated lighting devices as light sources to illuminate the flow field from different directions.

A Laser Doppler Vibrometer (LDV) Polytec PSV-100 is used to measure the hydrofoil vibrations according to the principle of heterodyne interferometer, with a beam of helium neon laser through the transparent bottom wall of the test section and scattered back. The measure point is selected in the mid-plane near the trailing edge of the hydrofoil ($x/c=0.8$) to reduce the influence of wall ef-

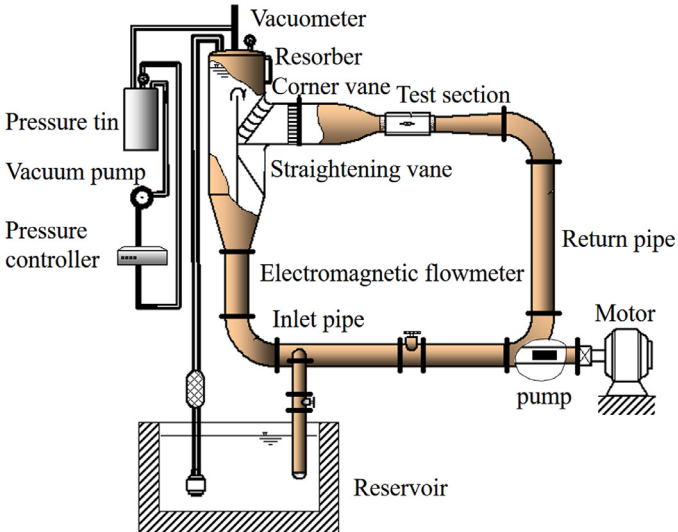


Fig. 1. Schematic of the cavitation tunnel.

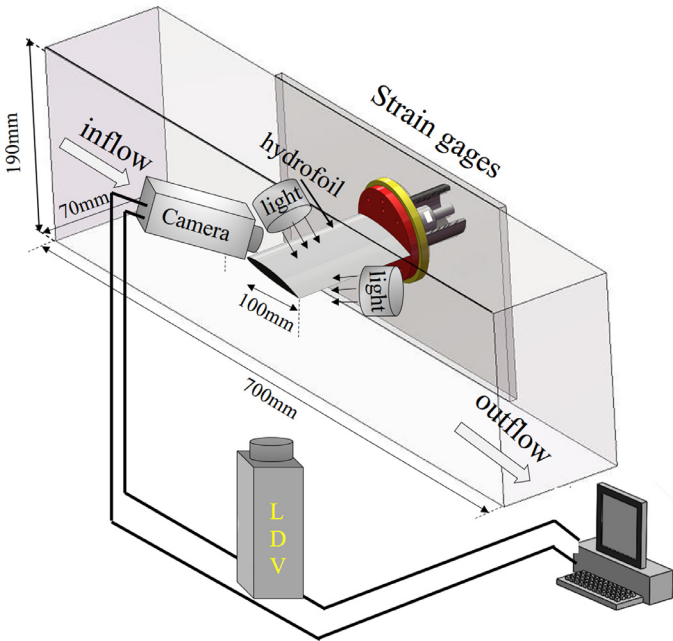


Fig. 2. Schematic of the experimental setup.

fect on the structure vibration. The frequency ranges from 0.5Hz to 22kHz and the velocity ranges from 0.05m/s to 0.5m/s. Then the velocity signal can be fed into digital inputs of a data acquisition system (NI X Series Multifunction Data Acquisition) whose largest sampling rate is 2.5M per channel, and 20.48 kHz is used in the present study, followed by a three-level 1-D wavelet analysis using the Haar wavelet (Strang and Nguyen, 1996) to de-noise the signal. A five components hydrodynamic load cell is applied to measure the lift and drag static force, the lift and drag precision is 1.5N and 0.5N respectively.

The modified NACA66 is applied in the this work, which is made of polyacetal (POM), with the density $\rho=1480\text{kg/m}^3$, modulus of elasticity $E=3\text{GPa}$, Poisson coefficient $\mu=0.35$. Tests are conducted at an initial angle of attack $\alpha_0=8^\circ$, with cavitation numbers, $\sigma=(p_\infty-p_v)/(0.5\rho U_\infty^2)$ ranging from 0.25 to 2.5, and Reynolds numbers, $Re=cU_\infty/\nu$ ranging from 5×10^5 to 10×10^5 , where c is the chord length $c=0.075\text{m}$, p_∞ is the tunnel pressure, p_v is the saturated vapor pressure, ν is the kinematic viscosity.

The foil is fixed at the back wall of the test section and there is a 1mm clearance between the free end of the hydrofoil and the front wall of the test section, so that the tip of which is free to deform.

3. Numerical model

3.1. Governing equations

The incompressible, unsteady Reynolds Average Navier-Stokes (URANS) equations without heat transfers and body force can be described as follow:

$$\frac{\partial(\rho_m)}{\partial t} + \frac{\partial(\rho_m u_j)}{\partial x_j} = 0 \quad (1)$$

$$\frac{\partial(\rho_m u_j)}{\partial t} + \frac{\partial(\rho_m u_i u_j)}{\partial x_j} = -\frac{\partial p}{\partial x_i} + \frac{\partial}{\partial x_j} \left[(\mu_m + \mu_t) \left(\frac{\partial u_i}{\partial x_j} + \frac{\partial u_j}{\partial x_i} \right) \right] \quad (2)$$

$$\rho_m = \rho_l \alpha_l + \rho_v \alpha_v \quad (3)$$

$$\mu_m = \mu_l \alpha_l + \mu_v \alpha_v \quad (4)$$

where ρ_l , ρ_v and ρ_m are the liquid, vapor and mixture densities, u is the velocity, p is the pressure, μ_l , μ_v and μ_m are the liquid, vapor and mixture laminar dynamic viscosity, μ_t is the turbulent viscosity, α_v is the vapor fraction, α_l is the liquid fraction. The subscripts i and j represent the direction of the Cartesian coordinates.

The $k-\omega$ SST turbulence model (Menter, 1993) is applied to solve the URANS equations in the present work, which uses the $k-\varepsilon$ modal far from the wall and $k-\omega$ modal near the wall. The turbulence viscosity μ_t is supplanted by μ_{t-mod} considering the influence of the local compressibility on the turbulence model (Coutier et al., 2003).

$$\frac{\partial(\rho_m k)}{\partial t} + \frac{\partial(\rho_m u_j k)}{\partial x_j} = P_k - D_k + \frac{\partial}{\partial x_j} \left[\left(\mu_m + \frac{\mu_t}{\sigma_k} \right) \frac{\partial k}{\partial x_i} \right] \quad (5)$$

$$\begin{aligned} \frac{\partial(\rho_m \omega)}{\partial t} + \frac{\partial(\rho_m u_j \omega)}{\partial x_j} &= C_\omega P_\omega - \beta_\omega \rho_m \omega^2 + \frac{\partial}{\partial x_i} \left[\left(\mu_m + \frac{\mu_t}{\sigma_k} \right) \frac{\partial \omega}{\partial x_i} \right] \\ &+ 2\rho_m (1 - F_1) \sigma_\omega^2 \frac{1}{\omega} \frac{\partial k}{\partial x_i} \frac{\partial \omega}{\partial x_i} \end{aligned} \quad (6)$$

$$\mu_t = \frac{\rho a_1 k}{\max(a_1 \omega; SF_2)}, \mu_{t-mod} = \mu_t f(n) \quad (7)$$

$$f(n) = \frac{\rho_v + (1 - \alpha_v)^n (\rho_l - \rho_v)}{\rho_v + (1 - \alpha_v)(\rho_l - \rho_v)} \quad (8)$$

Where k is the turbulent kinetic energy and ε is the dissipation. P_k P_ω are the production term of the turbulence, D_k is the dissipation term of the turbulence, $n=3$ is applied (Huang et al., 2013; Huang et al., 2014).

The Zwart cavitation model (Kubota et al., 1992) based on transport-equation is used in present study, which assumes that the size and density of cavitation nuclei keep constant.

$$\dot{m}^- = -C_{dest} \frac{3\alpha_{nuc}(1 - \alpha_v)}{R_B} \left(\frac{2}{3} \frac{p_v - p}{\rho_l} \right)^{1/2}, p < p_v \quad (9)$$

$$\dot{m}^+ = -C_{prod} \frac{3\alpha_v \rho_v}{R_B} \left(\frac{2}{3} \frac{p - p_v}{\rho_l} \right)^{1/2}, p > p_v \quad (10)$$

where α_{nuc} is the cavitation nuclei volume fraction, R_B is the bubble diameter, p_v is the saturated vapor pressure, C_{dest} is the

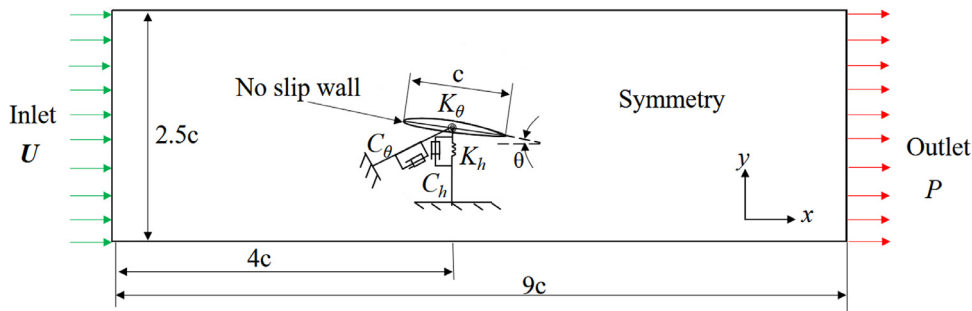


Fig. 3. Computational domain and boundary conditions.

rate for vapor generated from liquid when local pressure is lower than the vapor pressure. Conversely, C_{prod} is the rate for vapor back to liquid when local pressure is higher than the vapor pressure, the assumed model constants are the default values in CFX, $\alpha_{nuc} = 5 \times 10^{-4}$, $R_B = 1 \times 10^{-6} m$, $C_{dest} = 50$ and $C_{prod} = 0.01$.

3.2. Fluid-structure interaction algorithm

As for the solid model, the hydrofoil is simplified to a 2D model with bending and torsion. Both the twisting deformation θ and the bending displacement h are measured from the center of rotation along the elastic axis of the hydrofoil. The motion equation without excitation forces can be expressed as:

$$\begin{bmatrix} m & S_\theta \\ S_\theta & I_\theta \end{bmatrix} \begin{Bmatrix} \ddot{h} \\ \ddot{\theta} \end{Bmatrix} + \begin{bmatrix} C_h & 0 \\ 0 & C_\theta \end{bmatrix} \begin{Bmatrix} \dot{h} \\ \dot{\theta} \end{Bmatrix} + \begin{bmatrix} K_h & 0 \\ 0 & K_\theta \end{bmatrix} \begin{Bmatrix} h \\ \theta \end{Bmatrix} = \begin{Bmatrix} F \\ M \end{Bmatrix} \quad (11)$$

where m , S_θ , I_θ are the mass, static imbalance and inertia moment of the hydrofoil unit extension, respectively. K_h , K_θ are the structural bending and twisting stiffness coefficients. C_h and C_θ are the structural damping coefficients for the bending and twisting motions. h , h and \dot{h} are the bending displacement, velocity and acceleration of the hydrofoil, θ , $\dot{\theta}$ and $\ddot{\theta}$ are the torsional displacement, velocity and acceleration respectively. F and M are the fluid forces and moments acted on the hydrofoil.

The hybrid coupled fluid structure interaction algorithm ((Young et al., 2012) Wu et al., 2015) is used in this paper, which considers the influence of the virtual additional mass force with Theodorsen assumption (Theodorsen, 1935), so it can effectively avoid the over-prediction problem of the structural displacement:

$$\begin{bmatrix} m & S_\theta \\ S_\theta & I_\theta \end{bmatrix} \begin{Bmatrix} \ddot{h} \\ \ddot{\theta} \end{Bmatrix}_{n+1}^{i+1} + \begin{bmatrix} C_h & 0 \\ 0 & C_\theta \end{bmatrix} \begin{Bmatrix} \dot{h} \\ \dot{\theta} \end{Bmatrix}_{n+1}^{i+1} + \begin{bmatrix} K_h & 0 \\ 0 & K_\theta \end{bmatrix} \begin{Bmatrix} h \\ \theta \end{Bmatrix}_{n+1}^{i+1} - \begin{Bmatrix} F_{fluid}^T \\ M_{fluid}^T \end{Bmatrix}_{n+1}^{i+1} = \begin{Bmatrix} F \\ M \end{Bmatrix}_{n+1}^i - \begin{Bmatrix} F_{fluid}^T \\ M_{fluid}^T \end{Bmatrix}_{n+1}^i \quad (12)$$

where F_{fluid}^T and M_{fluid}^T are the potential flow estimate of the hydroelastic forces and moments, i is the sub-iteration number.

3.3. Numerical setup

The computational domain and boundary conditions are given in Fig. 3, according to the experimental setup. The velocity and pressure are set at the inlet and outlet respectively, according to the Reynolds number $Re = 6 \times 10^5$ and cavitation number $\sigma = 0.8$. The fluid mesh (shown in Fig. 4) consist of 140,000 elements and 70,000 nodes, which is refined near the leading and trailing edge of the foil, as well as in the wake region to ensure $y^+ = y \times \mu_\tau / v \approx 1$, where y is the distance from the first node away from the wall, μ_τ is the wall friction velocity. The numerical simulation uses a time step $\Delta t = 6 \times 10^{-3} s$ to ensure $CFL = \Delta t \times U_\infty / \Delta x \approx 1$.

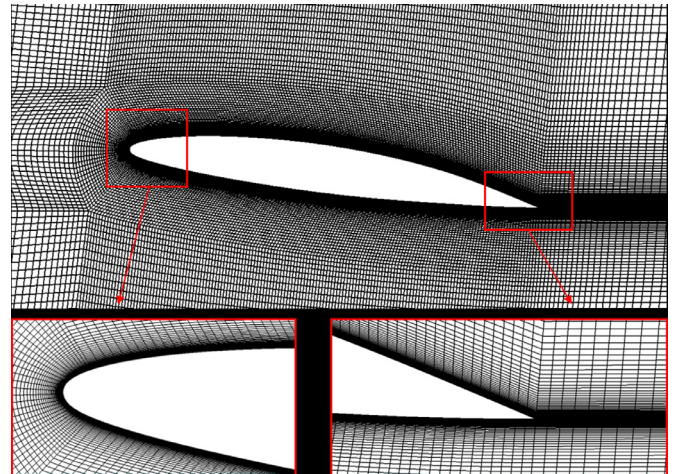


Fig. 4. Fluid mesh details.

4. Mode decomposition methodology

The POD and DMD methods are applied to extract the cavitating flow coherent structures around the flexible hydrofoil.

4.1. Proper orthogonal decomposition

Given a snapshot of the pressure field at N discrete moments, the entire flow field can be decomposed into the superposition of the basic flow and pulsation amount, namely,

$$P(x, t) = \bar{P}(x) + P'(x, t) \quad (13)$$

where $\bar{P}(x, t)$ is the mean part calculated by:

$$\bar{P}(x) = \frac{1}{N} \sum_{i=1}^N p(x, t_i) \quad (14)$$

and $P'(x, t)$ is the fluctuation part:

$$P'(x, t) = [p'(x, t_1), p'(x, t_2), \dots, p'(x, t_N)] \quad (15)$$

Assuming that the fluctuation part of the flow field can be decomposed into the product of the time coefficients $a_j(t_i)$ and the orthogonal eigenmodes ϕ_j ,

$$p'(x, t_i) = \sum_{j=1}^M a_j(t_i) \phi_j \quad (16)$$

where M is the modes number. Then the correlation matrix C can be expressed as:

$$C = P'(x, t)^T P'(x, t) C \phi_j = \lambda_j \phi_j \quad (17)$$

where λ_j and ϕ_j are the eigenvalues and eigenvectors of the matrix C , respectively. λ_j is information about the “weight” of eigenmodes. The main flow modes can be sorted according to the eigenvalue λ . The eigenvectors ϕ_j are defined as POD modes, which are orthonormal and the inner product between the modes satisfies

$$\langle \phi_i, \phi_j \rangle = \int_V \phi_i \bullet \phi_j dV = \begin{cases} 0, & i \neq j \\ 1, & i = j \end{cases} \quad (18)$$

then it can be calculated as:

$$a_j(t_i) = \langle p(x, t_i) - \bar{p}(x), \phi_j \rangle = \langle p'(x, t_i), \phi_j \rangle \quad (19)$$

the instantaneous pressure field at a certain time can be reconstructed by the time-averaged field, temporal coefficients, and POD modes:

$$p(x, t_i) = \bar{p}(x) + \sum_{j=1}^{N \text{ mode}} a_j(t_i) \phi_j \quad (20)$$

where N mode is the modes number selected for reconstructing the flow field. More details of the POD method can refer to Taira et al. (2017).

4.2. Dynamic mode decomposition

The data source mentioned above is presented in the form of matrix X and Y:

$$X = \{p(x, t_1), p(x, t_2) p(x, t_3) \dots p(x, t_{N-1})\} \quad (21)$$

$$Y = \{p(x, t_2), p(x, t_3) p(x, t_4) \dots p(x, t_N)\} \quad (22)$$

Supposing a linear mapping A between snapshots $p(x, t_i)$ and $p(x, t_{i+1})$,

$$p(x, t_i) = Ap(x, t_{i+1}) \quad (23)$$

then the matrix Y can be formulated as:

$$Y = [Ap(x, t_1), Ap(x, t_2) \dots, Ap(x, t_{N-1})] = AX \quad (24)$$

The DMD modes are related to the eigenvectors of A, however, it's difficult to compute A as the number of snapshots N is smaller than the mesh count of each snapshots k , so we require to find the matrix \tilde{A} to replace the high-dimensional matrix A, which can be obtained by singular value decomposition of X:

$$A = U\tilde{A}U^H \quad (25)$$

where $UU^H = I$, I is the unit matrix, and U can be obtained by the reduced SVD of X:

$$X = UQW^H \quad (26)$$

the calculation of matrix \tilde{A} can be seen as a minimization problem:

$$\tilde{A} = \underset{\tilde{A}}{\text{minimize}} \|Y - U\tilde{A}Q W^H\|_F^2 \quad (27)$$

where $\|\cdot\|_F^2$ is the Frobenius norm. A can be approximated to:

$$A \approx \tilde{A} = U^H Y W Q^H \quad (28)$$

Since matrix \tilde{A} is the optimal low-dimensional approximation matrix of Matrix A, the eigenvalue of Matrix \tilde{A} is a part of A, namely the Ritz eigenvalue. Defining the Ritz eigenvalue of the j-th mode as μ_j , the flow growth rate g_j and the frequency ω_j can be obtained through the logarithmic form of the eigenvalue:

$$g_j = \text{Re}\{\log(\mu_j)\}/\Delta t \quad (29)$$

$$\omega_j = \text{Im}\{\log(\mu_j)\}/\Delta t \quad (30)$$

The j-th dynamic mode is defined as:

$$\varphi_j = Uz_j \quad (31)$$

where z_j is the eigenvector corresponding to the j-th eigenvalue of matrix \tilde{A} . The dominant flow modes can be sorted by the norm of φ_j .

5. Results and discussions

5.1. Cavitation patterns associated with the structural vibrations

The measured mean values of lift coefficients and moment coefficients for the rigid and flexible hydrofoils as a function of σ at $\alpha = 8^\circ$, $Re = 10 \times 10^5$ are shown in Fig. 5(a) and (b). The results show that the trend of lift and moment coefficients for the rigid hydrofoil and the flexible one is approximately the same, the measured mean lift and moment coefficients slightly increase from incipient cavitation ($\sigma = 1.9$) to sheet cavitation ($\sigma = 1.5$), which is attributed to the increase in effective camber of the cavitating hydrofoil due to the increase of attached cavity changing the flow over the suction side of the hydrofoil (Young et al., 2018), despite minimum pressure limitations imposed by the cavity. After that, the measured mean lift and moment coefficients decrease significantly from sheet cavitation to cloud cavitation, which is because the minimum pressure limitation imposed by the cavity becomes more influential than the increased flow curvature, and the pressure on the pressure side decreases with the decrease of the cavitation number (Smith et al., 2020a). In addition, the flexibility accelerates the inflection point of the lift coefficient due to nose-up deformation. The obvious distinction for two hydrofoils is that the cloud cavitation of the flexible hydrofoil experienced a greater range of cavitation numbers, moreover, $\sigma = 1.94$ and $\sigma = 1.79$ are the upper σ limit of the incipient cavitation regime for the flexible hydrofoil and rigid hydrofoil, respectively. This indicates flexibility accelerates incipient cavitation and transition into the cloud cavitation while decelerated transition into the supercavitation. When the cavitation number is larger than 1.2, the lift and moment coefficients for the flexible hydrofoil are higher than the rigid hydrofoil, which is because the nose-up deformation causes the increase of effective angle of attack. This can be demonstrated by Fig. 6, it's obvious that the lift coefficients increase with the increase of the angle of attack.

The cavitation patterns of the flexible hydrofoil with different Re and σ are shown in Fig. 7. It can be observed that incipient cavitation, sheet cavitation, cloud cavitation, and supercavitation appear with the decrease of the cavitation number. With the cavitation number decreasing, incipient cavitation occurs near the leading edge of the hydrofoil. Furthermore, in the sheet cavitation, a thin layer of the cavity is attached on the suction side of the hydrofoil, accompanied with an unsteady trailing edge of the cavity. When the pressure further decreases, the trailing edge of the cavity becomes more unsteady, the large-scale cloud cavity is formed and shed periodically. When the cavitation number is further decreasing, the cavity is fully developed and the supercavity length is longer than the chord length.

Fig. 8 shows the measured normalized cavity length l/c , where l is defined as the maximum length of the attached cavity at the middle section of the hydrofoil, and corresponding normalized maximum vibration amplitude $A = 200 \times A_{\max}/c$ represented with the error bars in the separate symbols, where the A_{\max} is the maximum vibration amplitude of the measured position on the hydrofoil, at different cavitation stages. For all the cases with different Reynolds number, the cavity length increases with the decrease of σ . The vibration amplitude is relatively small for the incipient cavitation and sheet cavitation, while there is a significant growth of the vibration amplitude for the cloud cavitation. As the cavitation develops into the supercavitation, it drops down again but still slightly larger than that of the incipient cavitation and sheet cavitation.

As the cloud cavitation leads to more significant vibration, it is necessary to investigate the effect of cloud cavitation on the deformation, load coefficients of the hydrofoil. Fig. 9 shows the predicted transient evolution of the lift $C_l = L/0.5 \times$

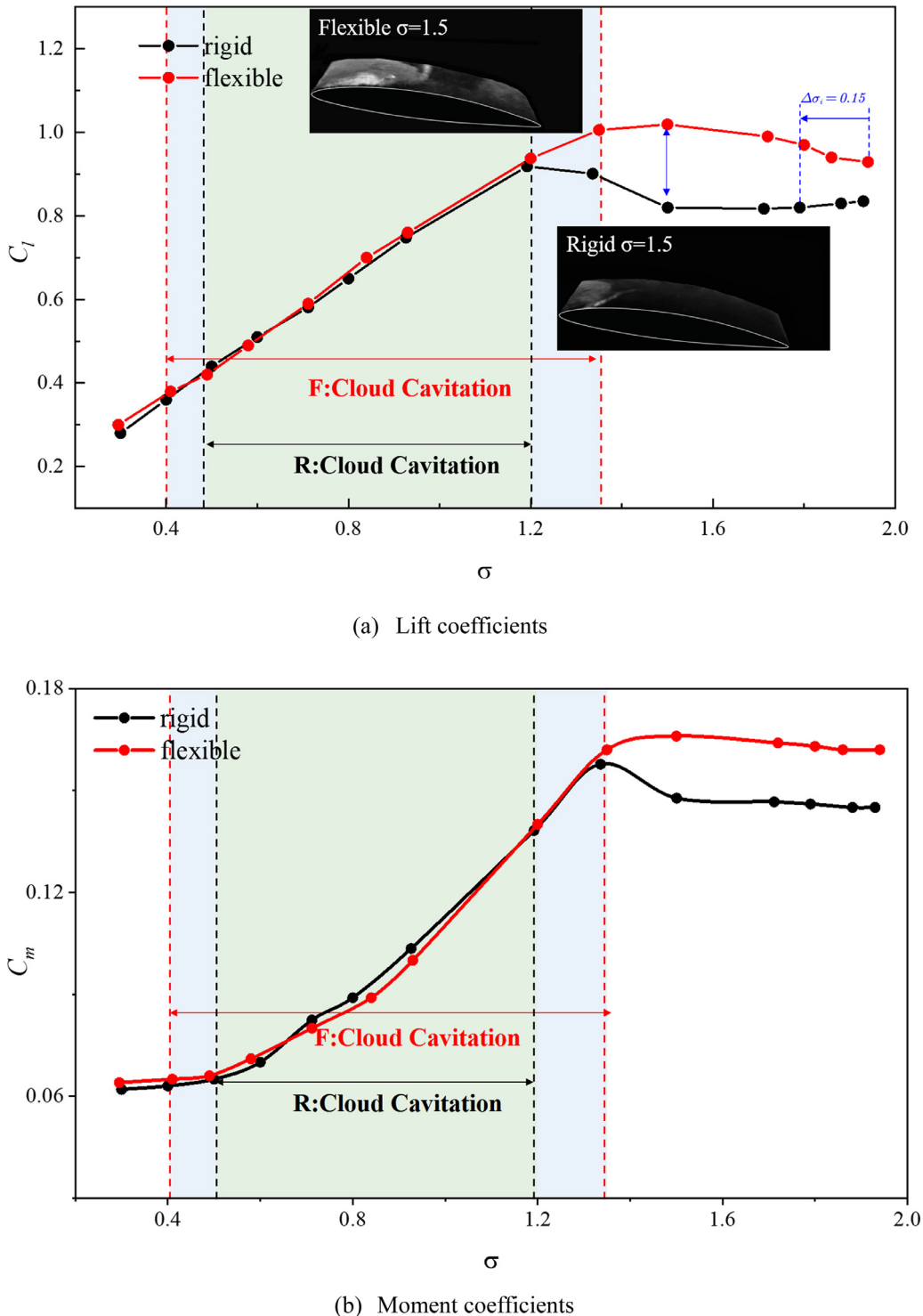


Fig. 5. Measured mean values of (a) lift coefficients and (b) moment coefficients as a function of σ experienced by the rigid and flexible hydrofoils at $\alpha = 8^\circ$, $Re = 10 \times 10^5$.

$\rho \times U_\infty^2 \times s \times c$, $\text{drag}C_d = D/0.5 \times \rho \times U_\infty^2 \times s \times c$ and moment $C_m = M/0.5 \times \rho \times U_\infty^2 \times s \times c^2$ coefficients, as well as predicted the bending (h) and twisting deformation (θ) associated with the vapor volume fraction (α), and vorticity contour (ω_z) at typical cloud cavitation case ($\sigma = 0.8$, $Re = 6 \times 10^5$), with positive vorticity values representing the counterclockwise vortex structures and the negative values representing the clockwise ones. Take one cycle (purple dotted box) as an example, at the beginning of a period, as shown in Fig. 9(a), the partial sheet cavity attaches to the hydrofoil suc-

tion side while the shedding cavity of the previous cycle still exists near the trailing edge of the hydrofoil. As shown in the temporal-spatial distribution of vapor volume fraction, seen in Fig. 9(f), the cavity grows from the leading edge to the trailing edge of the hydrofoil until $t_2 = t_0 + 30\%T_{cycle}$, accordant with the growth of the lift and drag coefficients, so the bending and twisting deformation are also enhanced. It should be noted that, during the development of the attached cavity, the re-entrant jet formed at the rear region of the cavity develops toward the leading edge, due to the

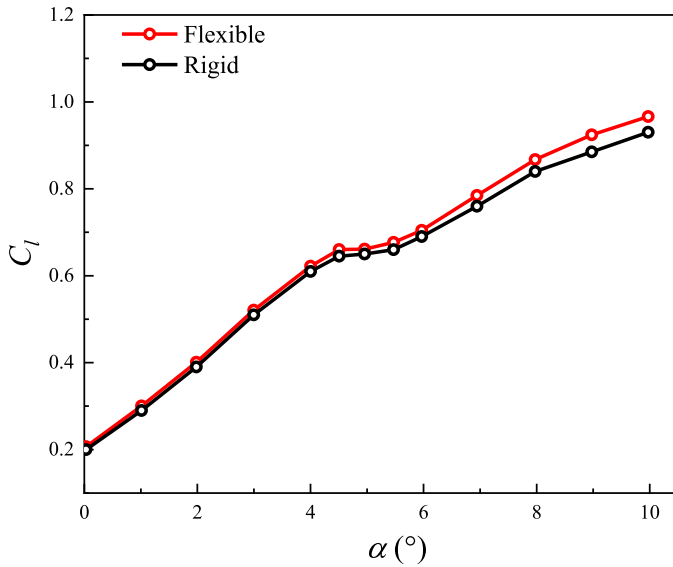


Fig. 6. Measured mean lift coefficients versus the angle of incidence of the rigid and flexible hydrofoils in subcavitating flow at $Re = 10 \times 10^5$.

strong reverse pressure gradient at the cavity closure, as shown in Fig. 9(b) and the white dot line in Fig. 9(f). In addition, the moment of re-entrant jet which effects the velocity and lasting time of the re-entrant jet mainly depends on the strength of the adverse pressure gradient in the cavitation closure region (Callenaere et al., 2001). At $t_3=t_0+60\%T_{cycle}$, the thickness of the cavity is sufficiently large to limit the interaction between the re-entrant jet and the cavity interface, so the re-entrant jet can reach the leading edge of the hydrofoil, pushing the cavity away from the wall and the rear region of the cavity is curled to form a large-scale cloud cavity, as shown in Fig. 9(c), the clockwise leading edge vortex(LEV) covers the entire suction side, interacting with the counter-clockwise trailing edge vortex(TEV), then two vortexes shed toward the trailing edge of the hydrofoil, causing the sharp fluctuation of the lift, drag and twisting deformation. At $t_4=t_0+80\%T_{cycle}$, as shown in Fig. 9(d), the cloud cavity totally sheds downstream. Clockwise and counterclockwise vortexes interact with each other on the middle of suction side then shed downstream of the foil. The shedding and

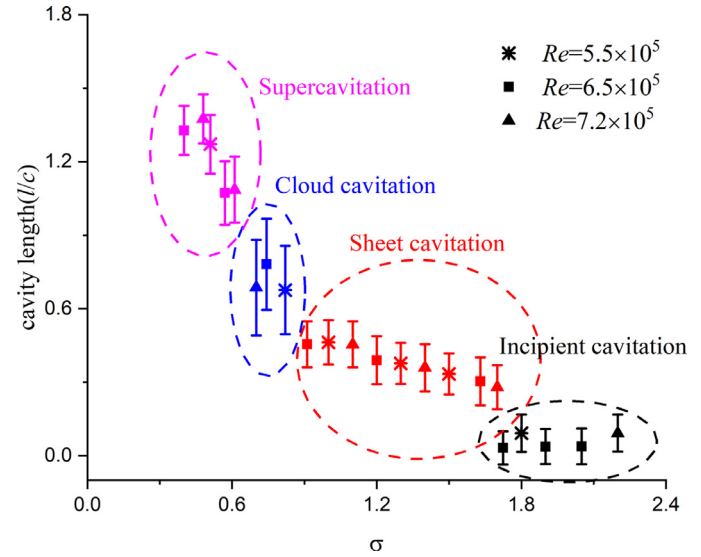


Fig. 8. Measured cavity length (the separate points) and the maximum vibration amplitude (the error bars) for different cavitation patterns.

collapse of the cavity resulting in the drop of lift, drag and bending deformation after t_4 as shown in Fig. 9(e).

From Fig. 9, it is the re-entrant jet that results to the cloud cavity shedding. To further analyze the shedding process, the pixels have been extracted from the mid-span, shown by a horizontal dashed red line in mean gray profile (Fig. 10 (a) and (b)). Several shedding process and the mean extend of the sheet cavity with its temporal behavior can be seen in the space-time diagram of the rigid hydrofoil (Fig. 11 (a)) and flexible hydrofoil (Fig. 11 (b)). A typical shedding process is annotated in space-time diagram of the rigid hydrofoil (Fig. 11 (c)), at the beginning of a shedding cycle, the partial sheet cavity attached to leading edge of hydrofoil begins to grow (shown in region ①), with the downstream end of the attached cavity shown by the yellow solid line. As the sheet cavity grows, a re-entrant jet forms between the foil surface and the cavity, then develops toward the leading edge (shown in region ②), when the re-entrant jet reaches the leading edge, the partial sheet cavity becomes thin, resulting

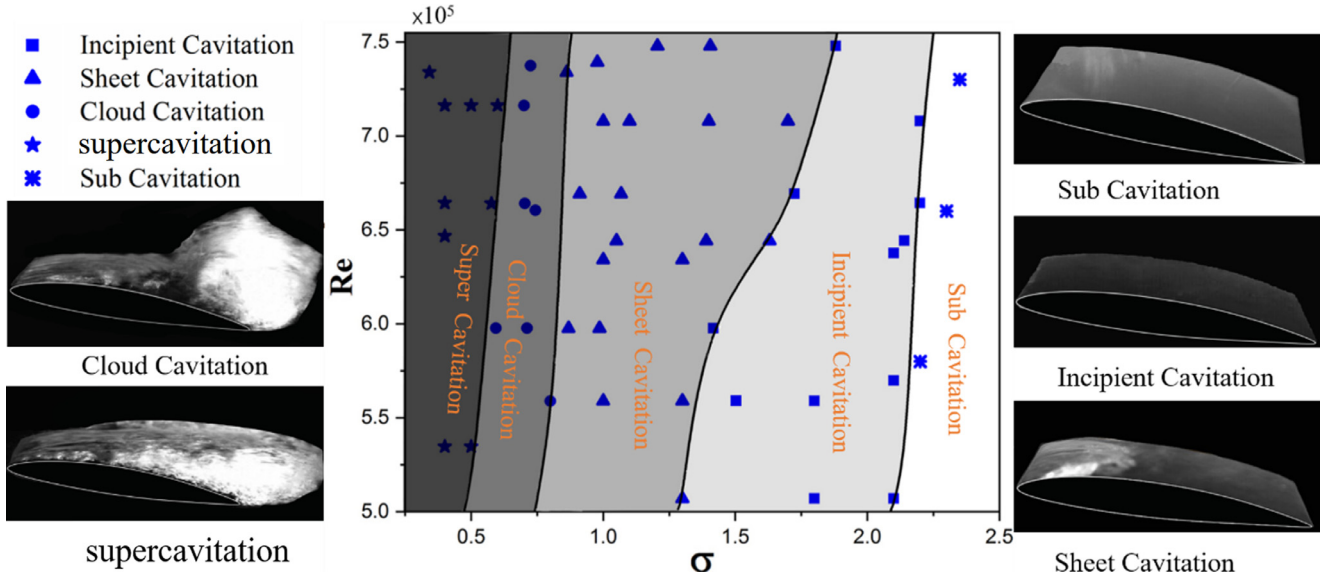


Fig. 7. Cavitation patterns for different Reynolds number Re and cavitation number σ .

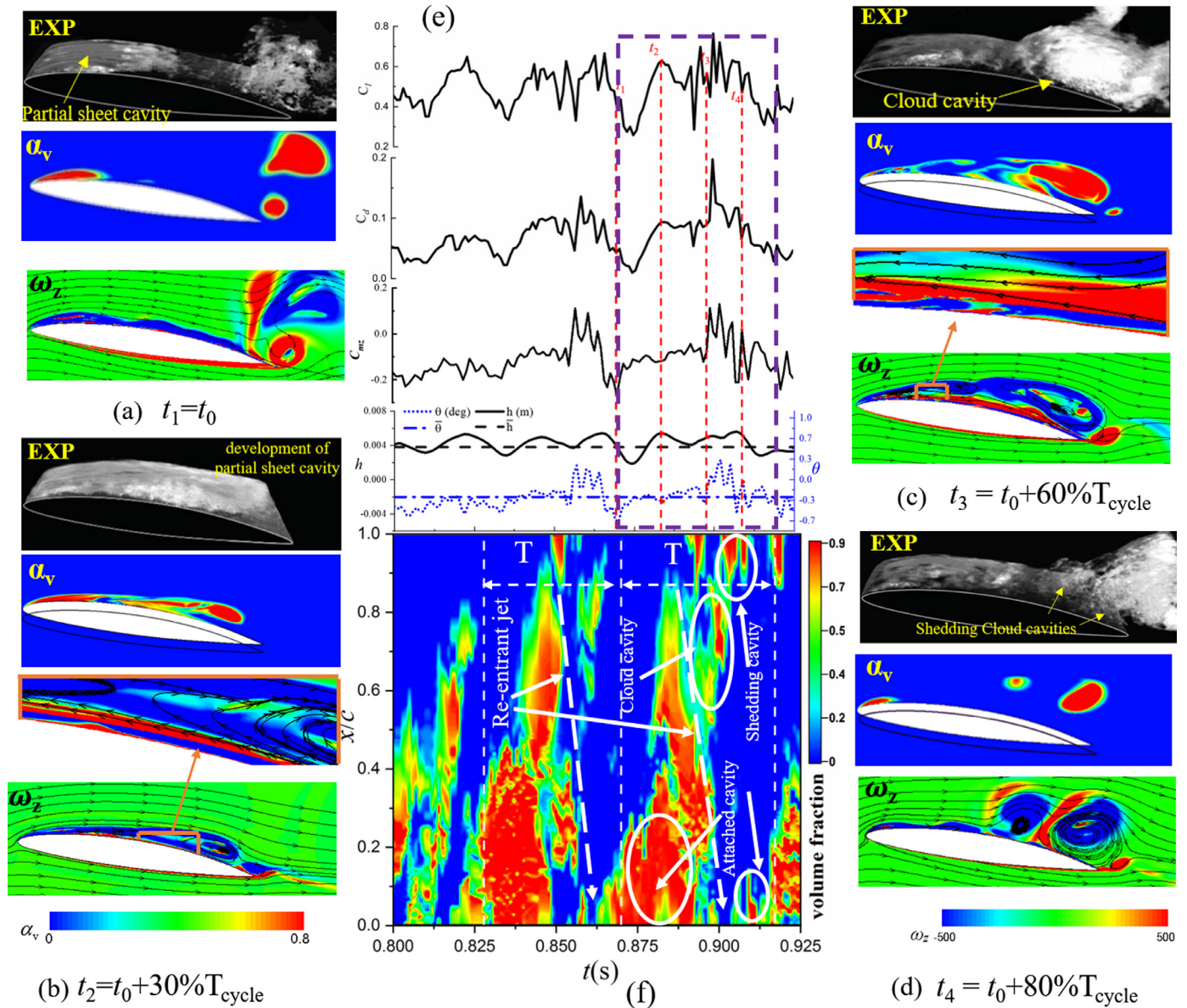


Fig. 9. Evolution of cloud cavitation patterns, vorticity contours, predicted load coefficients and deformations at $\sigma = 0.8$, $Re = 6 \times 10^5$.

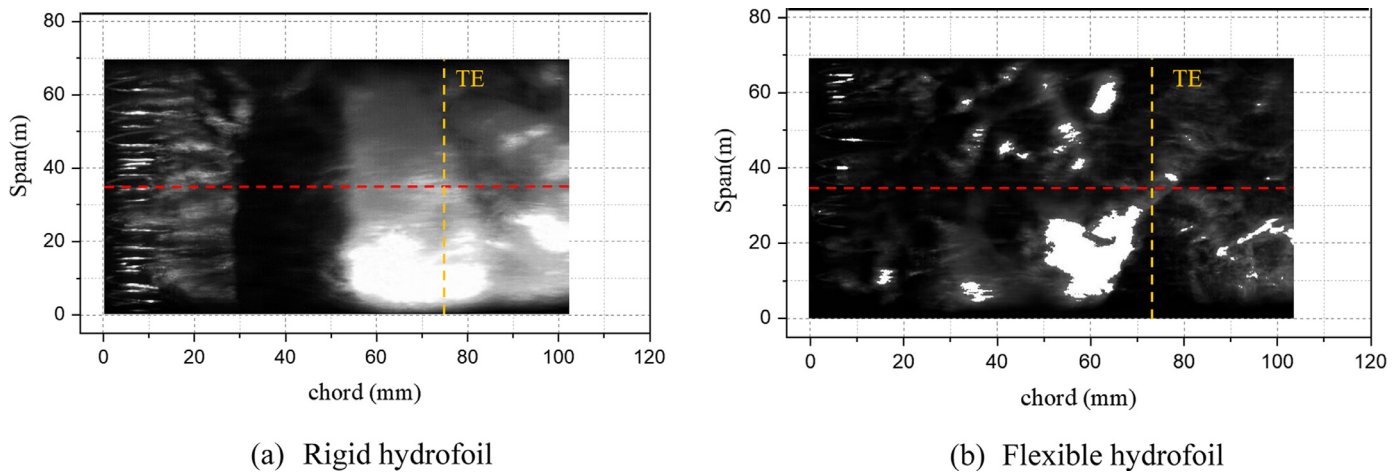


Fig. 10. Mean gray profile at a typical time for the rigid and flexible hydrofoil.

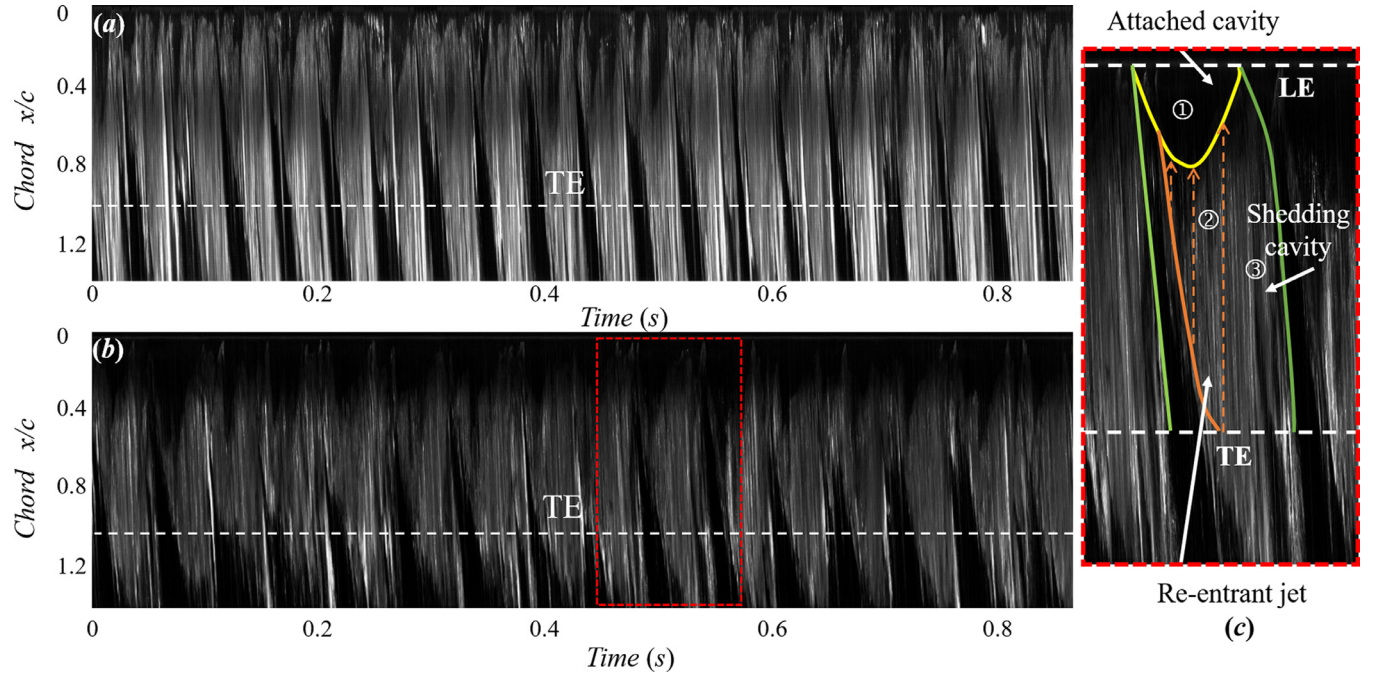


Fig. 11. Chordwise space–time diagram characteristic of the time dependence of the cavity of the rigid hydrofoil (a) and the flexible hydrofoil (b).

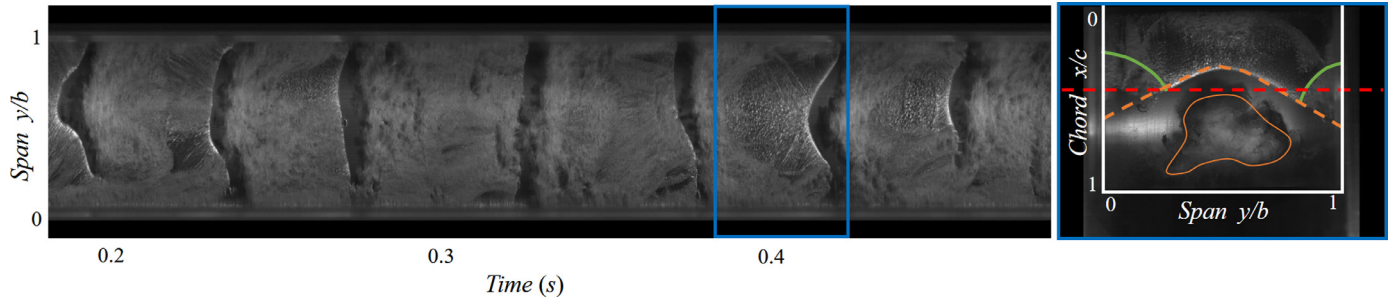


Fig. 12. Spanwise space–time diagram characteristic of the time dependence of the cavity of the flexible hydrofoil.

in break up of the cloud cavity, as shown in region ③, then the attached cavity of next shedding cycle begins to grow. Note that the small-scale vapor structures shed instead of a large-scale cloud cavity around the flexible hydrofoil, this is because the flexibility causes the obvious vibration, so the cavity is more fragmented. As shown in Fig. 11, it's obvious that the periodicity of flexible hydrofoil is more pronounced than rigid hydrofoil, and it has more cycles than the rigid hydrofoil in the same amount of time, which is corresponding to the cloud cavity shedding frequency of flexible hydrofoil with 22Hz and the rigid hydrofoil with 18Hz (Wu et al., 2018a). The increasing shedding frequency is because the average twisting angle is -0.287deg (be positive as the counter-clockwise direction), as shown in Fig. 9 (e), which results in nose-up twist deformation causing the increase in cavity length. The attached cavity of the flexible hydrofoil develops to its maximum degree earlier than that of the rigid one. In addition, because of the larger effective angle of attack caused by the nose-up twist deformation, the cavity inception of the next cavitation period is advanced.

Fig. 12 shows the spanwise cavity space–time diagram of the flexible hydrofoil, it is generated from a line of pixels extracted from $x/c=0.38$, shown by a horizontal dashed red line in some high-speed images. A typical time is annotated in a high-speed image shown in right part of the diagram. A significant spanwise variation can be observed with no uniform development of the attached cavity and the re-entrant jet, especially the uniform fea-

tures shown in the blue box. This complex behavior is due to multiple effects, which has been pointed out by previous researchers (Foeth et al., 2008; De Lange and De Bruin, 1998; Dang and Kuiper, 1999; Laberteaux and Ceccio, 2001). Firstly, the direction of the re-entrant jet is determined by the topology of the cavity closure line. The local direction of the re-entrant jet is nearly perpendicular to the cavity closure line locally. The cavity closure line is concave shown by the orange dashed line, so the re-entrant jet will diverge radially into the sheet cavitation. Besides, the cloud cavity shedding hindrance and the end wall effect are the probable reason, the moving and shedding of cloud cavity were no longer uniform spanwise, as shown in orange solid line, the previous shedding of cloud cavity sheds with a spindle shape, which hinders the grows of attached cavity in the middle span, so the attached cavity grows more rapidly at the two near-wall ends, with the side-entrant jets shown in green solid lines in Fig. 12.

The modal analysis is significant to investigate the vibration characteristics of the flexible hydrofoil. The experimental measurements are obtained by analyzing the vibration response to individual shock. Numerical predictions are obtained from the finite element analysis. Reasonable agreement has been acquired between the experimental and numerical results, and the prediction error for all modes are within 3.9%, which is presented in Table 1. The natural frequency in air and in water are compared in Fig. 13. It's found that the first three mode shapes are bending, twisting and

Table 1

The experiment and numerical natural frequency in still water.

Frequency in still water	Exp (Hz)	Num (Hz)	Error
Mode 1 (f_{w1})	102	98	3.9%
Mode 2 (f_{w2})	167	171	2.4%
Mode 3 (f_{w3})	213	215	0.9%

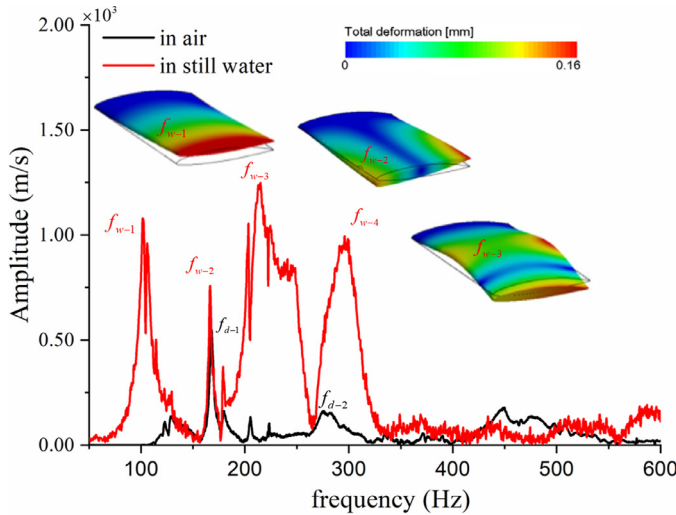


Fig. 13. The natural frequency in air and in water by the modal vibration test.

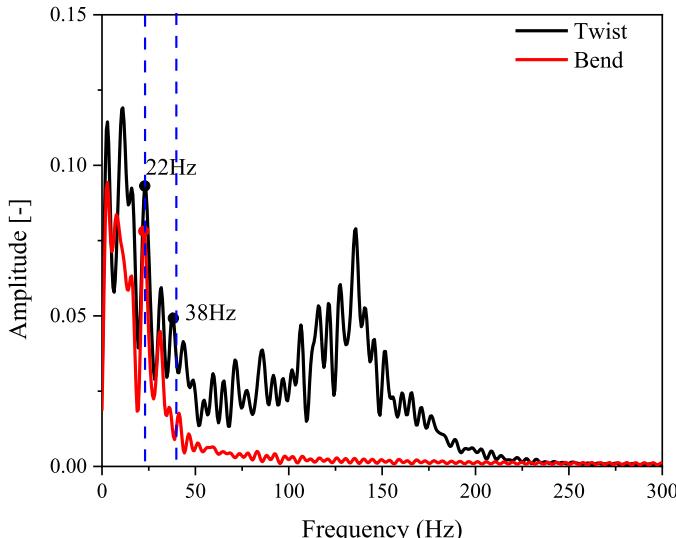


Fig. 14. Frequency spectrum of bending and twisting deformation for the flexible hydrofoil.

combined bending and twisting modes, respectively. The results show that the natural frequency in water is 65% lower than in air due to pronounced effect of added hydrodynamic mass in water.

To analyze the mechanism behind the effects of cavitation on the vibrations and vice versa in terms of the bending and twisting frequencies, the frequency spectrum plot of predicted bending and twisting deformation of flexible hydrofoil through the Fast Fourier Transform (FFT) and Lowpass filtering (LPF) is shown in Fig. 14, the amplitude is normalized by the absolute value of average of bending (0.0038 mm) and twisting deformation (0.005 rad). Because the deformation of the rigid hydrofoil is too small to measure, it is not presented here. It can be seen that both the bending and twisting deformation extract the 22 Hz, corresponding to the cavity shedding frequency f_{cav} (Wu et al., 2018a), which indicates that the cloud cavitation shedding has a significant influence on the foil deformation. On the other hand, the twisting deformation increases the effective angle of attack, advanced the cavity inception of the next period, resulting in a higher cavity shedding frequency of the flexible hydrofoil than that of the rigid hydrofoil. Overall, the cavitation has a significant effect on the vibrations and vice versa. Besides, the secondary frequencies of the torsional deformation include 38 Hz, while the bending deformation does not, which indicates that the vortex shedding has a significant influence on the twisting deformation.

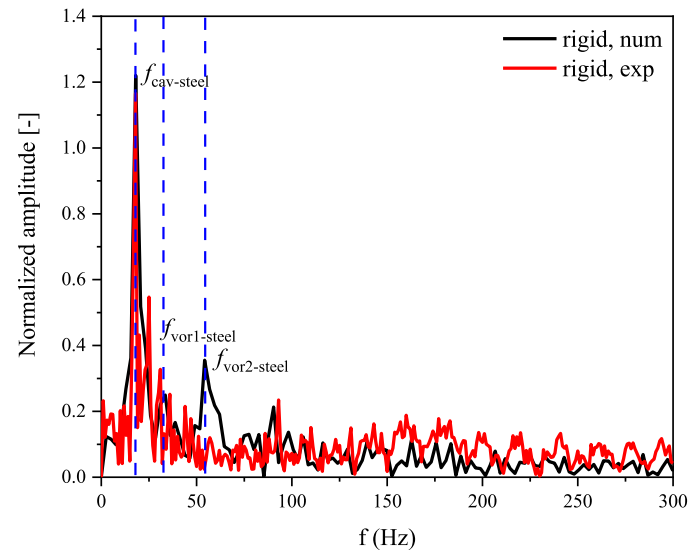


Fig. 15. Frequency spectrum of the vibration acceleration for cloud cavitation for the rigid hydrofoil.

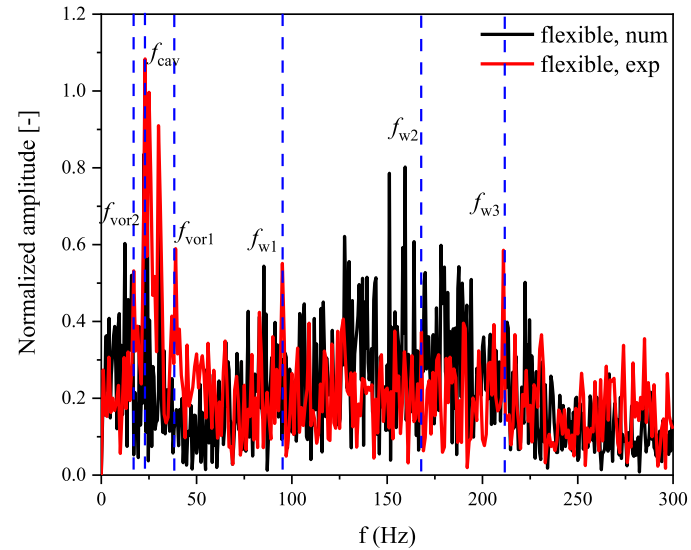


Fig. 16. Frequency spectrum of the vibration acceleration for cloud cavitation for the flexible hydrofoil.

To study the influence of the cavity on the hydrofoil vibration, the frequency spectrum plots of measured vibration acceleration and predicted lift of rigid and flexible hydrofoil through the Fast Fourier Transform are shown in Figs. 15 and 16, the vertical scale represents the power of the frequency in per unit spectral band. With the assumption that the lift is the main excitation source of the flow induced vibration, the spectral characteristics of the predicted vibration acceleration, which is computed from the differential of the LDV velocity, should be equivalent to that of predicted

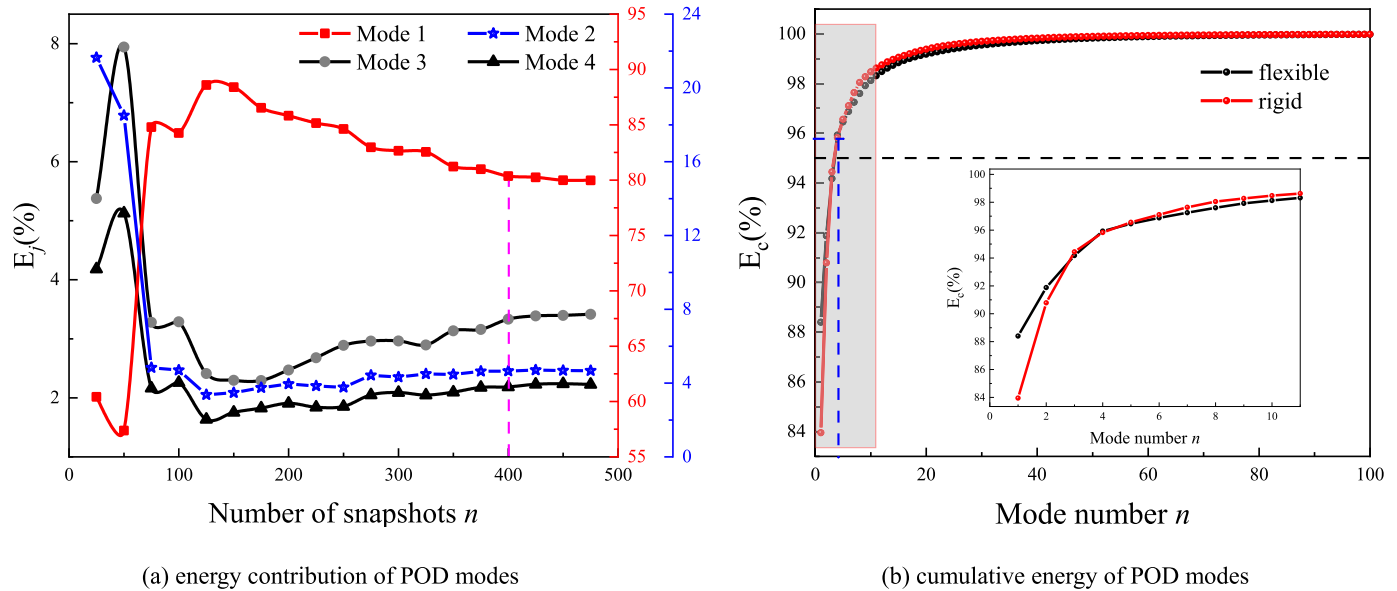


Fig. 17. Sensitivity analysis of POD modes.

lift imposed on the hydrofoil. In order to better compare the experimental and numerical results, the amplitude is normalized by the maximum value measured by the LDV system. It can be seen that the main cavitation-induced vibration frequency is about 18Hz and 22 Hz for the rigid and flexible hydrofoil, corresponding to the cavity shedding frequency f_{cav} (Wu et al., 2018a). It means that the cavity shedding dominates the vibration of the hydrofoil. Compared to rigid hydrofoil, the frequency spectrum of the flexible hydrofoil is more complex. The first three modal frequencies, the first and second bending frequency ($f_{w1}=102\text{Hz}$ and $f_{w2}=213\text{Hz}$) and the first twisting frequency ($f_{w3}=167\text{Hz}$) (Wu et al., 2018a), have also been captured. Besides, frequencies of 34Hz and 38Hz for the rigid and flexible hydrofoil are associated with the vortex shedding frequencies, which will be discussed in the following.

5.2. Decomposition of unsteady sheet/cloud cavitating flows

5.2.1. Assessment of POD method for decomposition of unsteady sheet/cloud cavitation

In order to extract the most energetic modes and significant coherent structures of the unsteady cloud cavitating flow, the POD method decomposes the original flow fields into low-order subspaces. The sensitivity of the POD analysis to the number of snapshots is applied in Fig. 17(a), showing the proportion of the first four modes of energy calculated as $E_j = \lambda_j / \sum_{j=1}^N \lambda_j$, where λ_j denotes the energy of j -th mode accounts for the total energy, and the snapshots are obtained every 50 time steps. Fluctuations of the energy can be observed with snapshots less than 100. When the number of snapshots $N > 400$, the energy of the first four modes almost has no change with the increase of the snapshots. So in this work, the pressure values of unsteady cloud cavitating field constitute a $K \times N$ matrix P , where K (number of mesh elements) = 54000 and N (snapshots counts) = 400. Fig. 17(b) presents the cumulative energy of the first 100 modes normalized by the entire energy of the 400 modes for the flexible hydrofoil, which are calculated as $E_c = \sum_{j=1}^n \lambda_j / \sum_{j=1}^N \lambda_j$. It can be seen that the most energetic mode of flexible hydrofoil occupies more than 88% of the total energy and the rigid one occupies 84%, and the energy of the subsequent modes decay as the slope of the curve decreases. The first four modes occupy 96% of the entire energy,

more than 95%, so they are mainly focused in the following analysis.

To further reveal the coherent flow structures of cavitating flow, Fig. 18 shows the dynamic mode contours of the first four POD modes for the rigid and flexible hydrofoils according to Eq. (17). As the mean flow field pressure is totally dislodged from the pressure field, the energy of each mode denotes the contribution of the pressure fluctuations. The activity of the first mode is confined to the lower portion of the chord with a high streamwise gradient behavior near the trailing edge of the hydrofoil on the suction side, suggesting that the first mode is related to the large-scale cloud cavity, and it occupies the most energy in the whole unsteady cavitating flow. Modes 2 has a distinct group of alternating positive and negative regions on the suction side, which indicates that as cloud cavity collapses and sheds, the trailing edge vortex structure grows due to mass transfer. That is to say, the area with high value of dynamic mode in Mode 2 represents the cloud cavity shedding, while that with low value of dynamic mode representing the trailing edge vortex (TEV), which indicates that as cloud cavity sheds downstream and collapses, TEV grows then dissipates periodically. From the third mode, we can attribute these contributions to the small-scale vortex structures with alternating positive and negative regions in the suction side. The first three modes clarify that various scales of the cavity and vortex structures are the dominant coherent structures that occupy a large amount of energy in the flow field. Besides, the most obvious distinction of POD modes between the rigid and flexible hydrofoil is the modes' scale. The modes' scale of flexible hydrofoil is smaller than that of rigid one, which is because the cloud cavity of flexible hydrofoil sheds in small-scale structures, which is in accordance with Fig. 10. In addition, the coherent structures of the third and fourth mode for the rigid hydrofoil is more regular, which is because the vibration of the rigid hydrofoil is not strong enough to destroy vortex structures.

Figs. 19 and 20 show the time evolution and frequency spectrum of the temporal coefficients of the first four modes for rigid and flexible hydrofoil according to Eq. (19). For the rigid hydrofoil, the periodicity of the temporal coefficients can be obviously observed for the first three mode with the dominant frequency of 18Hz, corresponding to the cloud cavity shedding frequency. Moreover, the secondary frequencies of 33Hz and 55Hz, corresponding

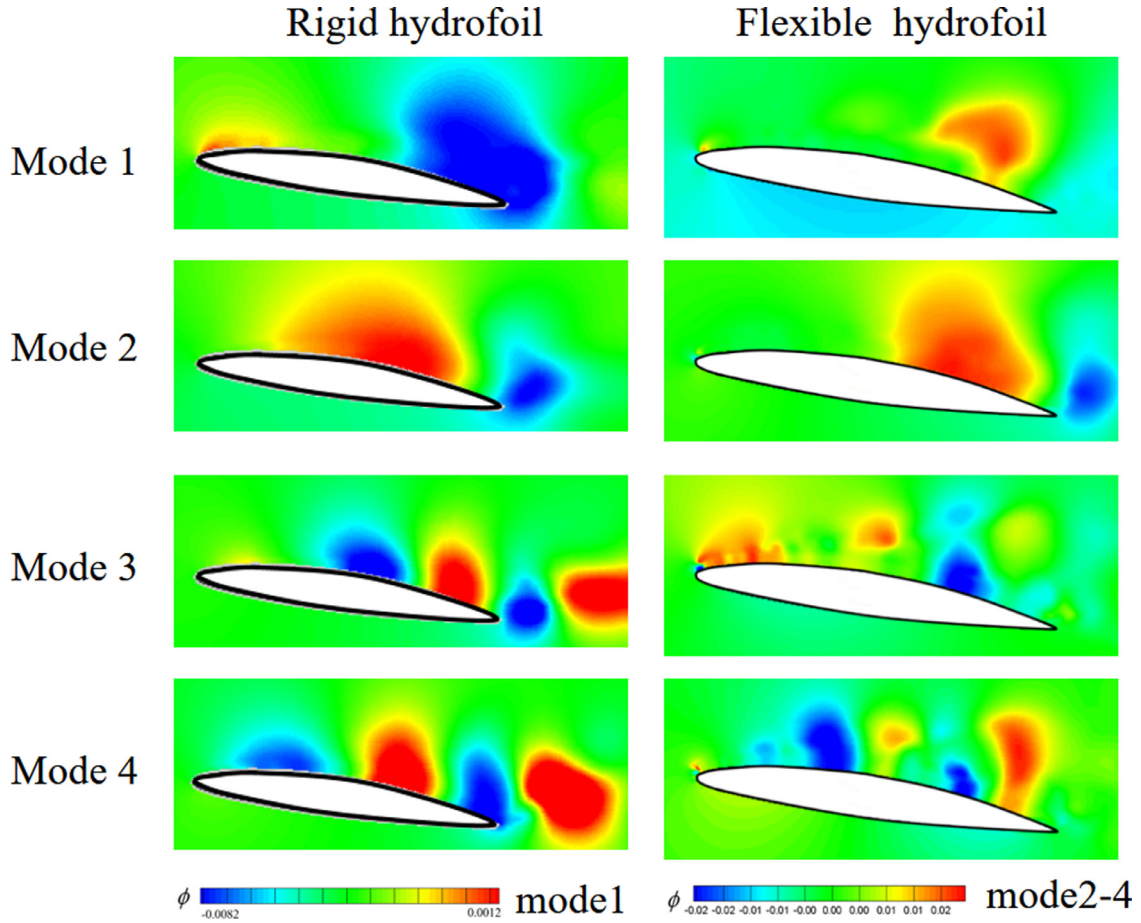


Fig. 18. First four energetic POD modes for cloud cavitation at $\sigma = 0.8$, $Re = 6 \times 10^5$.

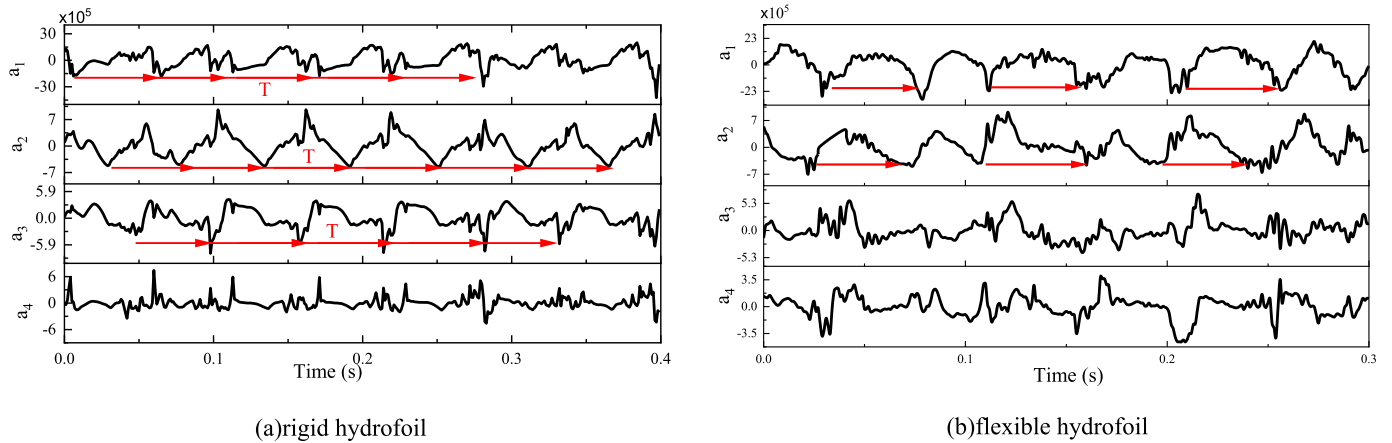
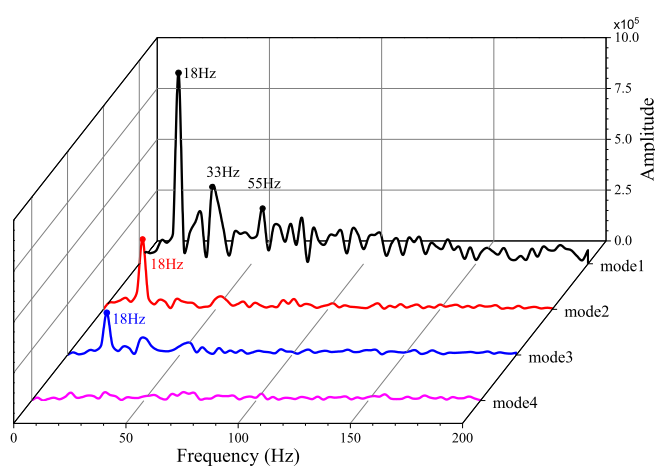


Fig. 19. Time evolution of the temporal coefficient.

to the vortex shedding frequency. For the flexible hydrofoil, the periodicity of the temporal coefficients can be obviously observed for the first mode, and slightly weakened for the second mode, with the dominant frequency of 22 Hz captured for the first and second modes. For the second mode, the secondary dominant frequency is 38Hz, corresponding to the vortex shedding frequency and we can further confirm that the second mode is related to interaction between the large-scale cavity and the trailing edge vortex shedding process. For the third and fourth modes, the periodicity is not

that strong compared with the first two modes, because the high-frequency and small-scale coherent structures has smaller effect on the pressure field. Moreover, the temporal coefficients of these modes have multiple harmonics, f_{cav} and $2f_{\text{cav}}$ harmonics, owing to the effect of multi-scale turbulence on the related modes.

To better illustrate the coherent, phase-resolved component and to analyze the evolution process of main coherent structures of the cloud cavitating flow, the mean and first four POD modes are combined to reconstruct the pressure field (Oudheusden et al., 2005).



(a) rigid hydrofoil

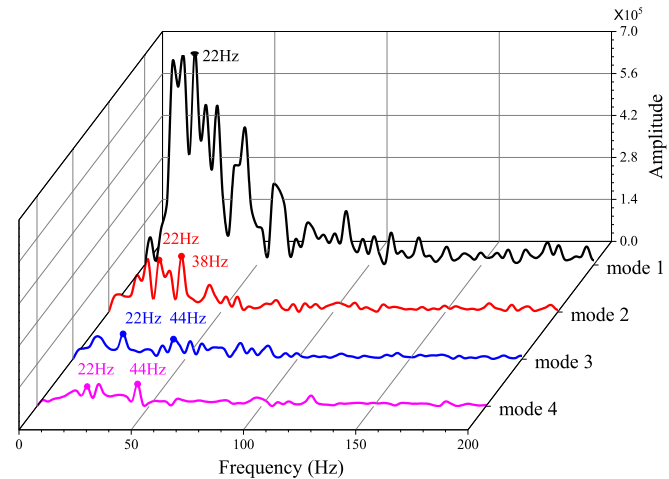
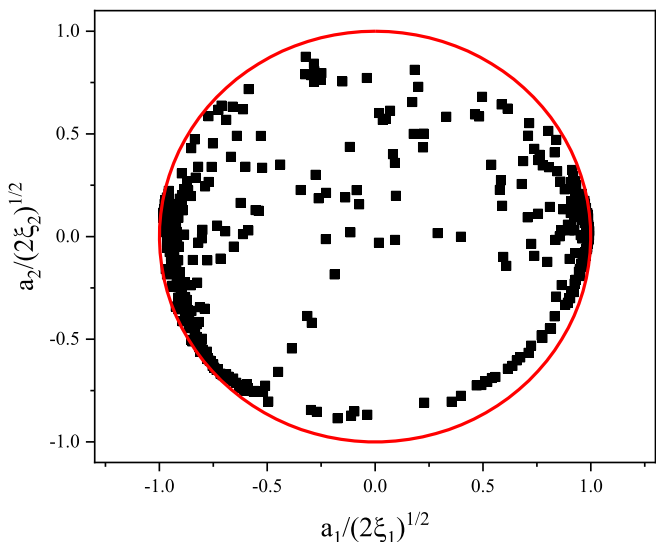
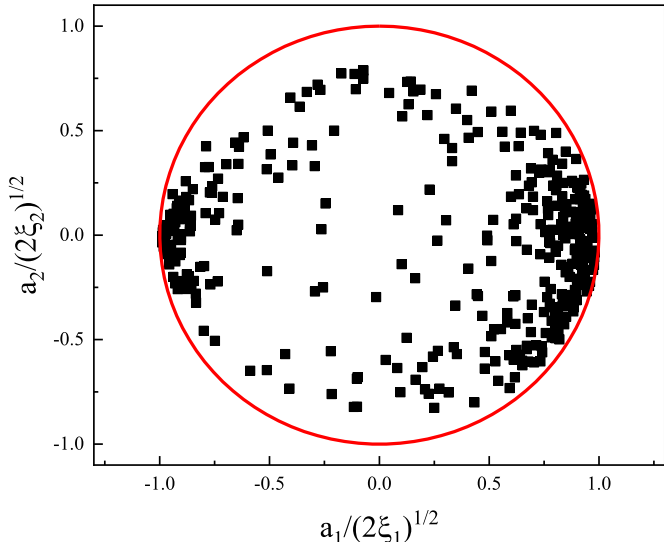


Fig. 20. Frequency spectrum of the temporal coefficients.



(a) rigid hydrofoil



(b)flexible hydrofoil

The reconstructed instantaneous flow fields seem like a spatial filter, they neglect small-scale turbulent fluctuations but retain the large-scale dominant flow features.

$$p_{LOM}(x, t_i) = \bar{p}(x) + a'_1(t_i) \cdot \phi_1(x) + a'_2(t_i) \cdot \phi_2(x) + a'_3(t_i) \phi_3(x) \\ + a'_4(t_i) \phi_4(x) \quad (32)$$

$$a'_1 = \sqrt{2\xi_1} \sin(t_i), a'_2 = \sqrt{2\xi_2} \cos(t_i) \quad (33)$$

$$\frac{a_1'^2}{2\xi_1} + \frac{a_2'^2}{2\xi_2} = 1 \quad (34)$$

Where p_{LOM} represents the low-order pressure field, $\sqrt{2\xi_1}$ and $\sqrt{2\xi_2}$ denote the amplitude of theoretical value of temporal coefficients a'_1 and a'_2 , respectively. The temporal coefficients of the first two modes show an azimuthal wave, which can be represented by two modes having a $\pi/2$ phase shift. Low-order model ignores the high-order harmonics of coherent motion and random turbulent motion contained in high-order modes.

According to Eq. (34), the theoretical temporal coefficients of the first two modes a'_1 and a'_2 are likely to form an ellipse in the (a'_1, a'_2) plane and show an azimuthal wave with a $\pi/2$ phase shift. Fig. 21 shows the cross plot of the temporal coefficients a'_1 and a'_2 for the rigid and flexible hydrofoil to verify that the first two modes denote the orthogonal constituents of fundamental coherent harmonic. The scatters on the theoretical curve indicate a periodical variation of cloud cavity shedding process, that around the theoretical curve represent the real temporal coefficients a_1 and a_2 , the discrepancies are due to the high-order harmonics of coherent motion and random turbulent motion contained in high-order modes. The most obvious distinction between the rigid and flexible hydrofoil lies in their location. The temporal coefficients of rigid hydrofoil are mainly distributed on the circle, by contrast, that of flexible hydrofoil mainly distributed around the circle, which is because that the cloud cavity of rigid hydrofoil sheds with a large-scale structure, its periodicity is stronger than flexible hydrofoil.

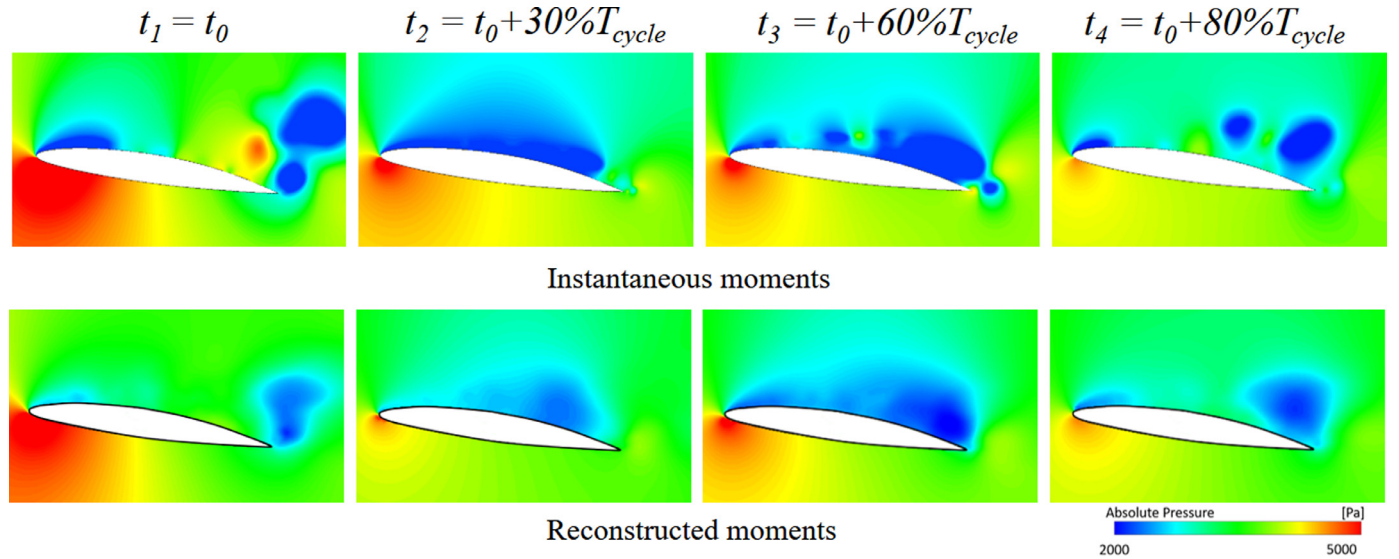


Fig. 22. Comparison of original pressure field and reconstructed pressure field.

With the mean pressure field and the first four modes, the reconstructed instantaneous flow fields are shown in Fig. 22 to analyze the evolution process of large-scale coherent structures. The formation, development and shedding of the large-scale attached cavity on the suction side of the hydrofoil has been well captured by the reconstructed field, while the small-scale structures have been ignored due to the low level of the energy contribution, although they still have significant effect on the cavitation development. This issue has also been mentioned by Miyanawala and Jaiman (2019).

5.2.2. Dynamic analysis of unsteady sheet/cloud cavitation via DMD method

To further investigate the dynamic characteristics of the cavitating flow around the flexible hydrofoil, the DMD method is used to extract the main frequency and the coherent structures of the flow field. According to the Eq. (28), the Ritz eigenvalues μ_j are applied to represent the stability of the modes, as shown in Fig. 23. The points inside the red cycle means that the growth rate $g_j < 0$ and the modes are convergence, those on the red circle are corresponding to periodical modes with $g_j = 0$, and the points outside the red circle represent that $g_j > 0$ and the modes are divergence. From Fig. 23, all the eigenvalues points for rigid and flexible hydrofoil are inside or on the red circle, which indicates that the modes are convergence modes or periodical modes.

The modes are sorted according to the norm of dynamic mode, as illustrated in Fig. 24. The horizontal axis is calculated by the ω_j according to Eq. (30). The vertical axis is calculated by the $\|\varphi_j\|$ according to Eq. (31), which describes the degree of coherence of the modes in the original flow field. For the rigid hydrofoil, the main peak frequencies are 18Hz (mode 2) and 34Hz (mode 4); for the flexible hydrofoil, the main peak frequencies are 22Hz (mode 2) and 38Hz (mode 4), which are in good agreement with the cavity shedding frequency and vortex shedding frequency. In addition, the frequency spectrum based on the numerical method cannot extract the 38Hz for the flexible hydrofoil, while the DMD method extracts the 38Hz and the associated dynamic modal characteristics, corresponding to the small-scale vortex structures. Fig. 25 shows the contours of first four modes for rigid and flexible hydrofoil calcu-

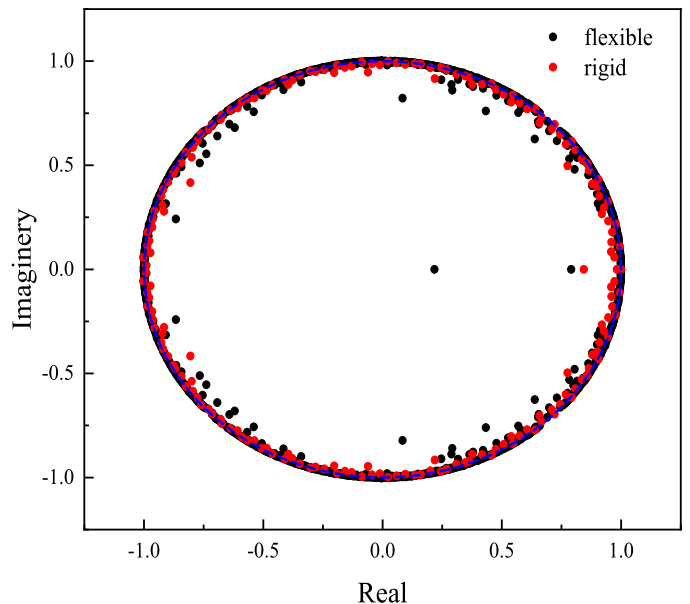


Fig. 23. Eigenvalues distribution for the rigid and flexible hydrofoil on the circle plane.

lated as the real part of the dynamic modes $\text{Re}(\varphi_j)$. Mode 1 represents the mean flow. The structures of mode 2 with the frequency of 22Hz for the flexible hydrofoil are similar to that of POD mode 1, which also attributes to cloud cavity shedding. It indicates that the most energetic structure is also the structure with the most important frequency in the flow field. While for the rigid hydrofoil, the structures of mode 2 are similar to that of POD mode 2, which are related to the interaction between the cloud cavity and the trailing edge vortex. Besides, the structures of mode 4 for the flexible hydrofoil are similar to that of POD mode 4, suggesting that these structures are related to the small-scale vortex structures with its frequency of 38Hz. The structures of mode 3 for the rigid hydrofoil are related to the small-scale vortex structures with its frequency of 10Hz. We can further substantiate that the

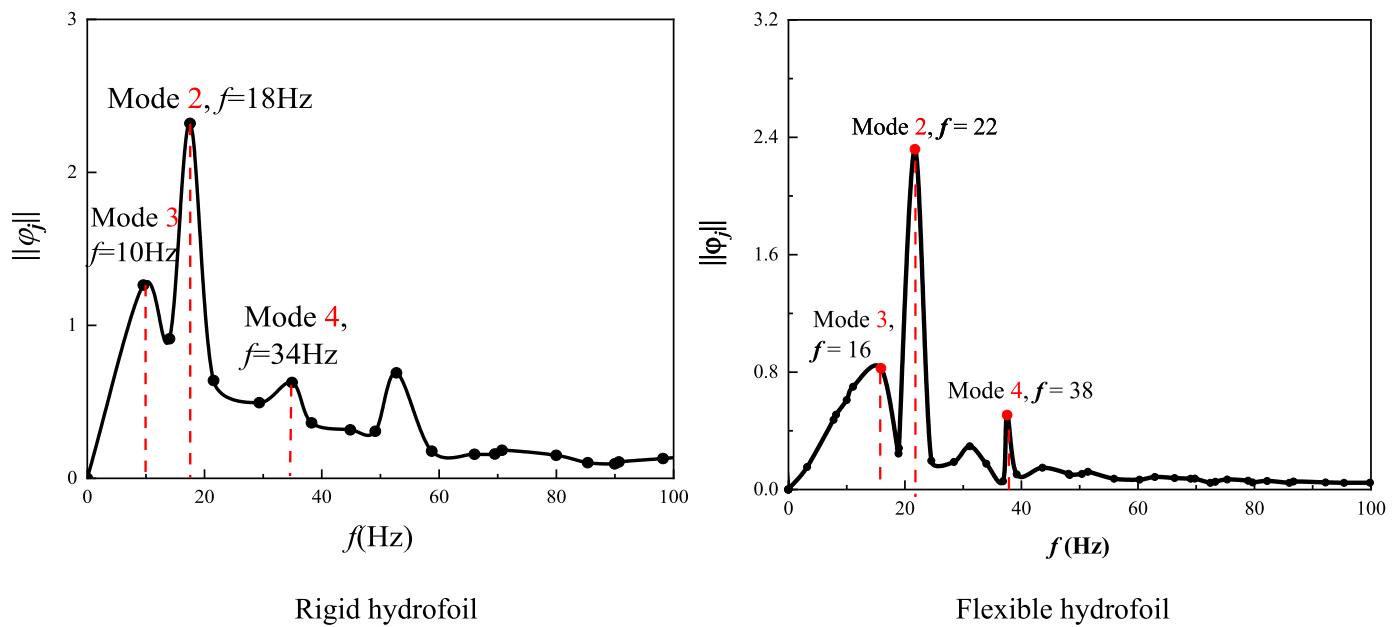


Fig. 24. Frequency spectrum of DMD modes for cloud cavitation at $\sigma = 0.8$, $Re = 6 \times 10^5$.

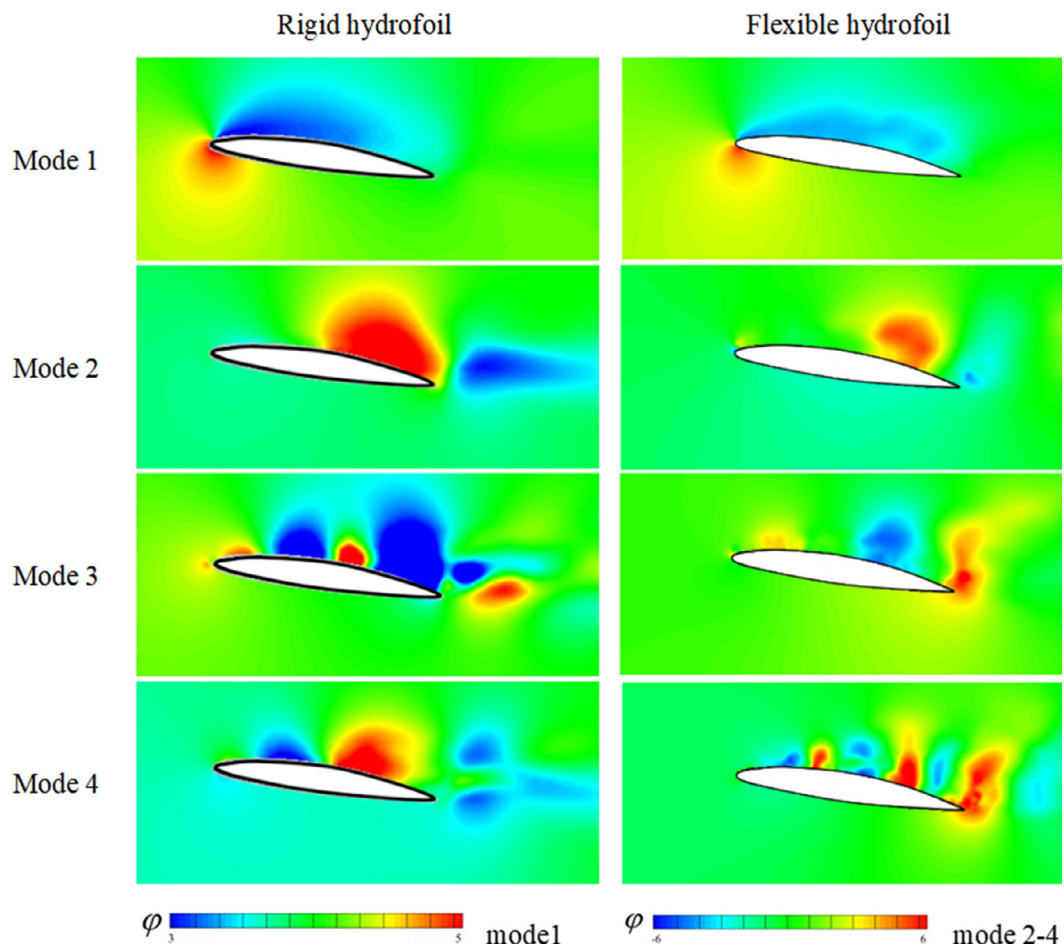


Fig. 25. First four energetic DMD modes for cloud cavitation at $\sigma = 0.8$, $Re = 6 \times 10^5$

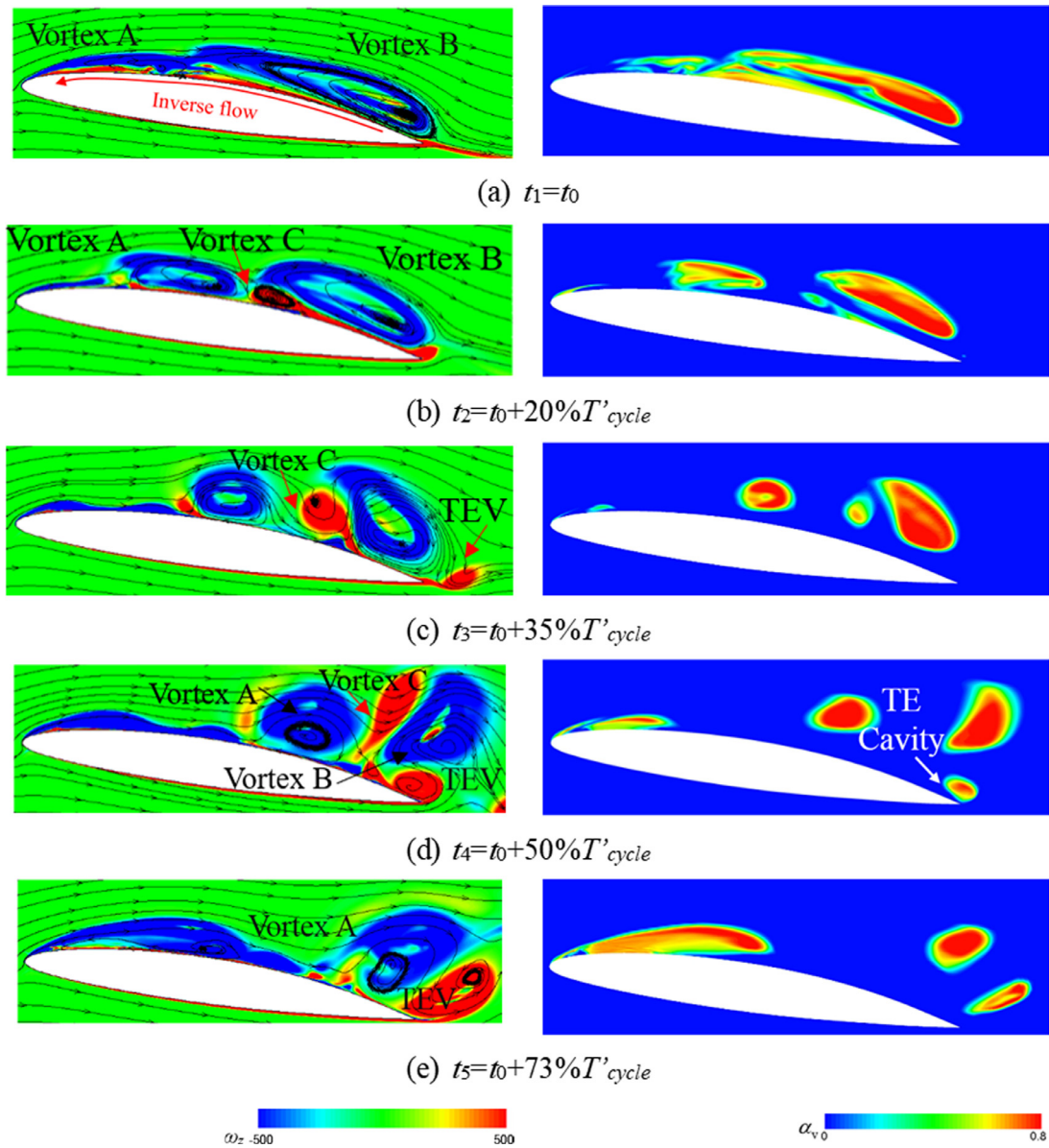


Fig. 26. Evolution of vortex shedding during one typical cavitation cycle.

process of vortex shedding is related to the dynamic characteristic of the flow field, although less energetic compared to the large cloud cavity shedding process. Like POD modes, the most obvious distinction between the rigid and flexible hydrofoil is the modes' scale.

5.3. Rigid hydrofoil Flexible hydrofoil

To further demonstrate the physical process related to mode 4 of the flexible hydrofoil, Fig. 26 and Fig. 27 show the evolution of vortex shedding and lift coefficient associated with the effective angle of attack during one cavitation cycle, respectively, where T'_{cycle} denotes the period of the vortex shedding process. As the adverse pressure gradient is strong enough to overcome the weaker momentum of the near-wall flow, a re-entrant jet is able to reach the leading edge of hydrofoil impinges on the cavity interface and leads to the shedding of cloud cavity, as well as the vortex structure in the core area of the cloud cavity, with two main part, vortex-A and vortex-B, as illustrated in Fig. 27(a). The

re-entrant jet moves upstream and the streamline flow attributes to a higher shear rate, so the formation of positive vorticity can be observed near the wall. Fig. 27(b) shows the detachment of cloud cavity and the interval of vortex A and vortex B increases, which allows enough space for the counterclockwise vortex C to develop. As shown in Fig. 27 (c), the counterclockwise vortex C develops further and a trailing edge vortex (TEV) due to the pressure difference between the suction and pressure side of the hydrofoil sheds downstream. From t_1-t_2 , a slight increase of twisting angle can be observed from Fig. 27, which is attributable to the increase of lift coefficient before t_2 . As shown in Fig. 27 (d), a clockwise TEV forms on the suction side again, the low internal pressure of which leads to the formation of the TE cavity. Meanwhile, the cloud cavity sheds downstream, together with complicated interaction between the clockwise and the counterclockwise vortices. As the cavitation further develops, the vortex-B sheds into the wake and followed by the clockwise vortex-A and the counterclockwise TEV. From t_2-t_5 , the average lift coefficient decreases due to the reduction of pressure differential between the suction side and the pressure side, which is attributable to vortices shedding downstream causing the

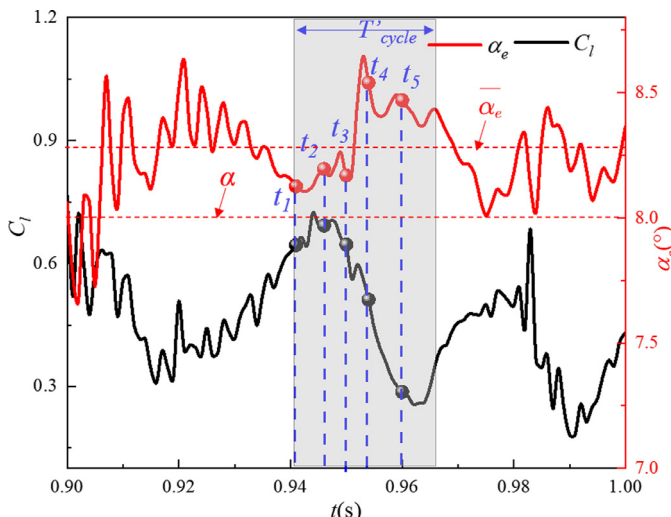


Fig. 27. Evolution of the lift coefficient and the effective angle of attack at $\sigma = 0.8$, $Re = 6 \times 10^5$.

increase of the pressure on the suction side. The decrease of twisting angle after t_4 is due to the decrease of lift coefficient from t_2-t_5 . Note that the phase of the twisting angle lags behind the lift coefficient, indicating that the twisting angle depending on the lift coefficient.

6. Conclusions

In this work, experimental and numerical methods, as well as the reduced order model are used to analyze the effect of flexibility on the cavitating flow structures and vibration characteristic, the complex discrepancy is presented by the comparison of a rigid and a flexible NACA66 hydrofoil. The primary finds are including:

- (1) Compared with rigid hydrofoil, the cloud cavitation of the flexible hydrofoil experienced a greater range of cavitation numbers in the measured lift and moment coefficients lines. The predicted cavitating behaviors have a good agreement with the measured observations. The cavity length goes up with the decrease of cavitation number and the vibration amplitude is greatest for the cloud cavitation. The unsteady cloud cavity sheds downstream due to the re-entrant jet rushing from the cavity closure to the leading edge. The uniformity of the growth of the attached cavitation along the spanwise is mainly attributed to the cloud cavity shedding hindrance and the end wall effect.
- (2) The influence of FSI on the cavitation behavior with the flexible hydrofoil is obvious. The cavitation development has affected the structural vibration frequency with the main peak corresponding to the cavity shedding frequency, the other two peaks are accordant with the vortex shedding frequencies induced by cavity, other three vibration frequencies related to the first three natural modes in still water; On the contrary, the deformation of the flexible hydrofoil has also affected the cavitating development, the cavity shedding frequency of which is increased due to the increasing effective angle of attack.
- (3) The POD method captured the most energetic modes of the pressure field, with the first two POD modes representing large-scale cavitating flow structures and the other two modes representing small-scale cavitating flow structures. The temporal coefficients of the first two modes show an azimuthal wave, which can be represented by two modes having a $\pi/2$ phase shift. The first four modes were used

to reconstruct the flow field and large-scale structures are captured while small-scale structures are ignored.

- (4) The DMD method accurately extracts the dominant frequency and modal characteristic of the flow field. The first mode represents the mean flow field, the second mode corresponds to large-scale vortex structures, the third and fourth modes are related to small-scale vortex structures. The vortex shedding frequency of 38Hz is well captured that the predicted method cannot extract. Like POD modes, the most obvious distinction between the rigid and flexible hydrofoil lies that the modes' scale of flexible hydrofoil is smaller than that of rigid hydrofoil, because the cloud cavity of the flexible hydrofoil sheds with small-scale due to its vibration.

7. Discussion and future work

It should be noted that the present work is inadequate, additional experimental and numerical investigations are needed. The experimental study is based on the FFT analysis on a one point laser vibration measurement, the position of the LDV would adjust to sweep more points along the surface of the hydrofoil to investigate the vibration distinction along the chordwise and spanwise. Also, the inadequacy of conventional turbulent model and cavitation model employed in the present simulation to capture the small-scale vortex structures and vibrations is inadequate. A more accurate model, which solves the small-scale structures and considers the cavity compressibility would help to improve the predictions. Besides, the effect of gap flow on the tip gap cavitation is ignored in current work, in the future, the effects of tip vortex cavitation on the dynamics of cavitation and vibration should be considered. High quality experiments are also needed with detailed measurement of the tip vortex cavitation and vibration velocity to validate the numerical models and better illuminate the underlying physics.

Declaration of Competing Interest

None.

CRediT authorship contribution statement

Yunqing Liu: Conceptualization, Methodology, Software, Validation, Formal analysis, Investigation, Resources, Data curation, Writing - original draft, Writing - review & editing, Visualization, Supervision, Project administration, Funding acquisition. **Qin Wu:** Software, Writing - review & editing, Supervision, Funding acquisition. **Biao Huang:** Writing - review & editing, Supervision, Funding acquisition. **Hanzhe Zhang:** Software, Investigation. **Wendong Liang:** Software, Investigation. **Guoyu Wang:** Supervision, Funding acquisition.

Acknowledgments

The authors gratefully acknowledge the support by the National Natural Science Foundation of China (Nos. 51839001, 51909002, 52079004), Beijing Natural Science Foundation (Nos. 3204056, 3212023), Defense Industrial Technology Development Program (JCKY2018203B025).

References

- Alenius, E., 2014. Mode switching in a thick orifice jet, an LES and Dynamic Mode Decomposition approach. *Comput. Fluids* 90, 101–112.
- Arndt, R.E.A., 1981. Cavitation in fluid machinery and hydraulic structures. *Annu. Rev. Fluid Mech.* 13 (1), 273–326.
- Batchelor, G.K., 1967. *An Introduction to Fluid Dynamics*. Cambridge University Press, New York.

- Callenaere, M., Franc, J.P., Michel, J.M., Riondet, M., 2001. The cavitation instability induced by the development of a re-entrant jet. *J. Fluid Mech.* 444, 223–256.
- Chae, E.J., Akcabay, D.T., Lelong, A., et al., 2016. Numerical and experimental investigation of natural flow-induced vibrations of flexible hydrofoils. *Phys. Fluids* 28 (7), 075102.
- Che, B.X., Cao, L.L., Chu, N., et al., 2019. Dynamic behaviors of re-entrant jet and cavity shedding during transitional cavity oscillation on NACA0015 hydrofoil. *J. Fluids Eng.- Trans. ASME* 141 (6).
- Coutier, D.O., Reboud, J.L., Delannoy, Y., 2003. Numerical simulation of the unsteady behavior of cavitating flows. *Int. J. Numer. Methods Fluids* 42 (5), 519–530.
- Dang, J., Kuiper, G., 1999. Re-entrant jet modeling of partial cavity flow on three dimensional hydrofoils. *J. Fluids Eng.* 121 (4), 781–787.
- De Lange, D., De Bruin, G., 1998. Sheet cavitation and cloud cavitation, re-entrant jet and three-dimensionality. *Appl. Sci. Res.* 58 (1), 91–114.
- Ducoin, A., Jacques, André Astolfi, Gobert, M.L., 2012a. An experimental study of boundary-layer transition induced vibrations on a hydrofoil. *J. Fluids Struct.* 32, 37–51.
- Ducoin, A., Astolfi, J.A., Sigrist, J.F., 2012b. An experimental analysis of fluid structure interaction on a flexible hydrofoil in various flow regimes including cavitating flow. *Eur. J. Mech. B. Fluids* 36, 63–74.
- Ducoin, A., Young, Y.L., 2013. Hydroelastic response and stability of a hydrofoil in viscous flow. *J. Fluids Struct.* 38, 40–57.
- Foeth, E.-J., van Terwesga, T., van Doorn, C., 2008. On the collapse structure of an attached cavity on a three-dimensional hydrofoil. *J. Fluids Eng.* 130 (7), 071303.
- Harwood, C.M., Felli, M., Falchi, M., et al., 2019. The hydroelastic response of a surface-piercing hydrofoil in multiphase flows. Part 2. Modal parameters and generalized fluid forces. *J. Fluid Mech.* 884 (A3), 1–59.
- Huang, B., Qiu, S.C., Li, X.B., et al., 2019. A review of transient flow structure and unsteady mechanism of cavitating flow. *J. Hydodyn. Ser. B (English Ed.)* 31 (3), 429–444.
- Huang, B., Young, Y.L., Wang, G.Y., et al., 2013. Combined experimental and computational investigation of unsteady structure of sheet/cloud cavitation. *J. Fluids Eng.* 135 (7), 1–16.
- Huang, B., Zhao, Y., Wang, G.Y., 2014. Large eddy simulation of turbulent vortex-cavitation interactions in transient sheet/cloud cavitating flows. *Comput. Fluids* 92, 113–124.
- Ji, B., Luo, X., Wu, Y., et al., 2013. Numerical analysis of unsteady cavitating turbulent flow and shedding horse-shoe vortex structure around a twisted hydrofoil. *Int. J. Multiph. Flow* 51, 33–43.
- Kubota, A., Kato, H., Yamaguchi, H., 1992. A new modelling of cavitating flows: a numerical study of unsteady cavitation on a hydrofoil section. *J. Fluid Mech.* 240, 59–96.
- Laberteaux, K., Ceccio, S., 2001. Partial cavity flows. Part 2. Cavities forming on test objects with spanwise variation. *J. Fluid Mech.* 431, 43–63.
- Lelong, A., Guifant, P., Astolfi, J.A., 2018. An experimental analysis of the structural response of flexible lightweight hydrofoils in cavitating flow. *J. Fluids Eng. Trans. ASME* 140 (2), 021116.
- Leroux, J.B., Coutier-Delgosha, O., Astolfi, J.A., 2005. A joint experimental and numerical study of mechanisms associated to instability of partial cavitation on two-dimensional hydrofoil. *Phys. Fluids* 17 (5).
- Li, M., Tan, L., Cao, S.L., 2019. Dynamic mode decomposition of cavitating flow around ALE 15 hydrofoil. *Renewable Energy*, 139: 214–227.
- Liang, W.D., Chen, T.R., Wang, G.Y., et al., 2020. Investigation of unsteady liquid nitrogen cavitating flows with special emphasis on the vortex structures using mode decomposition methods. *Int. J. Heat Mass Transfer* 157, 119880.
- Menter, F.R., 1993. Improved two-equation K omega turbulence models for aerodynamic flows. NASA Technical Memorandum 103975, 1–31.
- Miyanawala, T.P., Jaiman, R.K., 2019. Decomposition of wake dynamics in fluid-structure interaction via low-dimensional models. *J. Fluid Mech.* 867, 723–764.
- Oudheusden, B.W.V., Scarano, F., Hinsberg, N.P.V., et al., 2005. Phase-resolved characterization of vortex shedding in the near wake of a square-section cylinder at incidence. *Exp. Fluids* 39 (1), 86–98.
- Pan, C., Xue, D., Wang, J., 2015. On the accuracy of dynamic mode decomposition in estimating instability of wave packet. *Exp. Fluids* 56 (8), 164.
- Peng, X.X., Ji, B., Cao, Y., et al., 2016. Combined experimental observation and numerical simulation of the cloud cavitation with U-type flow structures on hydrofoils. *Int. J. Multiph. Flow* 79, 10–22.
- Pelz, P.F., Keil, T., Gro, T.F., 2017. The transition from sheet to cloud cavitation. *J. Fluid Mech.* 817, 439–454.
- Peters, A., Lantermann, U., Moctar, O., 2018. Numerical prediction of cavitation erosion on a ship propeller in model- and full-scale. *Wear* 408–409, 1–12.
- Prothrin, S., Billard, J.Y., Djeridi, H., 2016. Image processing using proper orthogonal and dynamic mode decompositions for the study of cavitation developing on a NACA0015 foil. *Exp. Fluids* 57 (10), 157.
- Saito, Y., Takami, R., Nakamori, I., et al., 2007. Numerical analysis of unsteady behavior of cloud cavitation around a NACA0015 foil. *Comput. Mech.* 40 (1), 85–96.
- Smith, S.M., Venning, J.A., Pearce, B.W., et al., 2020a. The influence of fluid-structure interaction on cloud cavitation about a flexible hydrofoil. Part 1. *J. Fluid Mech.* 896.
- Smith, S.M., Venning, J.A., Giosio, D.R., et al., 2018. Cloud cavitation behavior on a hydrofoil due to fluid-structure interaction. *J. Fluids Eng.* 141 (4).
- Smith, S.M., Venning, J.A., Pearce, B.W., et al., 2020b. The influence of fluid-structure interaction on cloud cavitation about a flexible hydrofoil. Part 2. *J. Fluid Mech.* 897.
- Strang, G., Nguyen, T., 1996. Wavelets and filter banks. *J. Korean Soc. Ind. Appl. Math.* 1 (9), 603–654.
- Sun, T., Wei, Y., Zou, L., et al., 2019. Numerical investigation on the unsteady cavitation shedding dynamics over a hydrofoil in thermo-sensitive fluid. *Int. J. Multiph. Flow* 111, 82–100.
- Taira, K., Brunton, S.L., Dawson, S.T.M., et al., 2017. Modal analysis of fluid flows: an overview. *AIAA J.* 55, 1–29.
- Theodorsen, T., 1935. General theory of aerodynamic instability and the mechanism of flutter. *Naca 496*, 291–313.
- Vinha, N., Meseguer, G.F., De Vicente, J., et al., 2016. A dynamic mode decomposition of the saturation process in the open cavity flow. *Aerospace Sci. Technol.* 52, 198–206.
- Wang, C.C., Wu, Q., Huang, B., et al., 2018a. Numerical investigation of cavitation vortex dynamics in unsteady cavitating flow with shock wave propagation. *Ocean Eng.* 156, 424–434.
- Wang, G.Y., Wu, Q., Huang, B., 2017. Dynamics of cavitation-structure interaction. *Acta Mech. Sin.* 33 (4), 685–708.
- Wang, G.Y., Senocak, I., Shyy, W., et al., 2001. Dynamics of attached turbulent cavitating flows. *Prog. Aerospace Sci.* 37 (6), 551–581.
- Wang, Z.Y., Zhang, M.D., Decai, K., et al., 2018b. The influence of ventilated cavitation on vortex shedding behind a bluff body. *Exp. Therm. Fluid Sci.* 98, 181–194.
- Wu, Q., Huang, B., Wang, G.Y., et al., 2015. Experimental and numerical investigation of hydroelastic response of a flexible hydrofoil in cavitating flow. *Int. J. Multiph. Flow* 74, 19–33.
- Wu, Q., Wang, Y.N., Wang, G.Y., 2017. Experimental investigation of cavitating flow-induced vibration of hydrofoils. *Ocean Eng.* 144, 50–60.
- Wu, Q., Huang, B., Wang, G.Y., et al., 2018a. The transient characteristics of cloud cavitating flow over a flexible hydrofoil. *Int. J. Multiph. Flow* 99, 162–173.
- Wu, Q., Wang, C.C., Huang, B., et al., 2018b. Measurement and prediction of cavitating flow-induced vibrations. *J. Hydodyn.* 30 (6), 774–781.
- Wu, X.C., Wang, Y.W., Huang, C.G., 2016. Effect of mesh resolution on large eddy simulation of cloud cavitating flow around a three-dimensional twisted hydrofoil. *Eur. J. Mech. B. Fluids* 55, 229–240.
- Yang, J., Xie, T., Liu, X.H., et al., 2019. Study of unforced unsteadiness in centrifugal pump at partial flow rates. *J. Therm. Sci.*
- Young, Y.L., Chae, E.J., Akcabay, D.T., 2012. Hybrid algorithm for modeling of fluid-structure interaction in incompressible, viscous flows. *Acta Mech. Sin.* 28(4), 1030–1041.
- Young, Y.L., Garg, N., Brandner, P.A., et al., 2018. Load-dependent bend-twist coupling effects on the steady-state hydroelastic response of composite hydrofoils. *Compos. Struct.* 189, 389–418.